

Science from a glimpse: Hubble SNAPshot observations of massive galaxy clusters

Repp A. & Ebeling H.

Institute for Astronomy, University of Hawaii, 2680 Woodlawn Drive, Honolulu, HI 96822, USA

MNRAS **479**, 844–864 (2018)

ABSTRACT

Hubble Space Telescope SNAPshot surveys of 86 X-ray selected galaxy clusters at $0.3 < z < 0.5$ from the MACS sample have proven invaluable for the exploration of a wide range of astronomical research topics. We here present an overview of the four MACS SNAPshot surveys conducted from Cycle 14 to Cycle 20 as part of a long-term effort aimed at identifying exceptional cluster targets for in-depth follow up by the extragalactic community. We also release redshifts and X-ray luminosities of all clusters observed as part of this initiative. To illustrate the power of SNAPshot observations of MACS clusters, we explore several aspects of galaxy evolution illuminated by the images obtained for these programmes. We confirm the high lensing efficiency of X-ray selected clusters at $z > 0.3$. Examining the evolution of the slope of the cluster red sequence, we observe at best a slight decrease with redshift, indicating minimal age contribution since $z \sim 1$. Congruent to previous studies’ findings, we note that the two BCGs which are significantly bluer ($\geq 5\sigma$) than their clusters’ red sequences reside in relaxed clusters and exhibit pronounced internal structure. Thanks to our targets’ high X-ray luminosity, the subset of our sample observed with *Chandra* adds valuable leverage to the X-ray luminosity–optical richness relation, which, albeit with substantial scatter, is now clearly established from groups to extremely massive clusters of galaxies. We conclude that SNAPshot observations of MACS clusters stand to continue to play a vital pathfinder role for astrophysical investigations across the entire electromagnetic spectrum.

Key words: surveys – gravitational lensing: strong – galaxies: evolution – galaxies: clusters: general – galaxies: elliptical and lenticular, cD – X-rays: galaxies: clusters

1 INTRODUCTION

Massive clusters ($M \gtrsim 10^{15} M_{\odot}$, $L_X \gtrsim 10^{45} \text{ erg s}^{-1}$, $0.1\text{--}2.4 \text{ keV}$, $\sigma \gtrsim 1000 \text{ km s}^{-1}$) are extremely rare systems that constitute sensitive probes of cosmological parameters even at modest redshifts (e.g., Mantz et al. 2008, 2010a, 2014). As the largest and most massive gravitationally bound systems in the Universe, they also represent ideal laboratories for astrophysical studies of the interactions and properties of dark matter, gas, and galaxies (e.g., Markevitch et al. 2004; Bradač et al. 2008; Merten et al. 2011; Ebeling et al. 2014; von der Linden et al. 2014; Harvey et al. 2015) as well as for investigations into the evolution of brightest cluster galaxies (BCGs), the most luminous stellar aggregations in the Universe (e.g., Quillen et al. 2008; Hlavacek-Larrondo et al. 2012; Stott et al. 2012; Werner et al. 2014; Green et al. 2016). Clusters also play a central role in attempts to trace large-scale cosmic flows to distances well beyond those accessible to galaxy surveys (e.g., Lauer & Postman 1994; Hudson & Ebeling 1997; Kocevski et al. 2007; Kashlinsky et al. 2010; Planck Collaboration et al. 2014). Finally, and importantly, massive clusters act as extremely powerful gravitational telescopes that allow us to detect and characterize distant background galaxies out to redshifts that would otherwise be inac-

cessible to observation (see Kneib & Natarajan 2011 for a review). As a result, the most massive galaxy clusters (and among these the most distant ones) are prized targets for a wide range of extragalactic research.

X-ray luminous clusters have proven to be the most powerful gravitational ‘lenses’, since they are – by virtue of the X-ray selection process – three-dimensionally bound, rarely affected by projection effects, and intrinsically massive (e.g., Horesh et al. 2010). In addition, the frequency of strong-lensing features increases dramatically with cluster redshift (Meneghetti et al. 2003). Consequently, the cluster targets of choice have been provided by the Massive Cluster Survey (MACS; Ebeling et al. 2001, 2007, 2010; Mann & Ebeling 2012). Like its counterparts at lower redshift, the BCS and REFLEX (Ebeling et al. 1998, 2000; Böhringer et al. 2004), MACS uses X-ray selection and optical follow-up observations to identify galaxy clusters among the tens of thousands of X-ray sources detected in the *ROSAT* All-Sky Survey (RASS; Voges et al. 1999; Böller et al. 2016). By focusing exclusively on systems at $z > 0.3$ and surveying a vast solid angle (in excess of $22,000 \text{ deg}^2$), MACS pursued a singular goal: a comprehensive search for the rarest, most massive clusters (Fig. 1; see Ebeling et al. 2001 for more details). Thanks to the very large solid angle covered, MACS

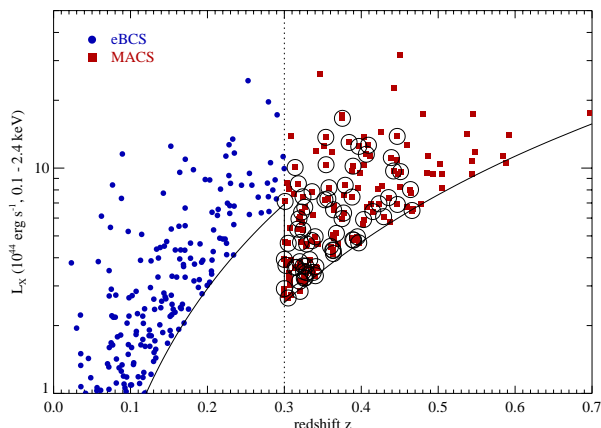


Figure 1. X-ray flux limited cluster samples compiled from RASS data. Limited to systems at $z > 0.3$, the MACS sample contains many of the most X-ray luminous (and hence most massive: Stanek et al. 2006; Reichert et al. 2011; Zhang et al. 2017) clusters in the universe. Clusters circled in black have been observed as part of our *HST* SNAPshot programmes and are the subject of this paper.

(like the *Planck* cluster sample; Planck Collaboration et al. 2016) is complementary to cluster surveys covering tens, hundreds, or a few thousand square degrees; the latter, which include groundbased surveys exploiting the Sunyaev-Zel’dovich effect (Sunyaev & Zel’dovich 1972) using, for instance, the South Pole Telescope or the Atacama Cosmology Telescope (Williamson et al. 2011; Marriage et al. 2011), primarily probe the population of average-mass clusters, due to the much smaller solid angles covered.

We here provide an overview of an observational programme that unites two valuable resources: the MACS legacy sample of the most massive clusters in the Universe at $z > 0.3$, and the unparalleled resolution and sensitivity of the *Hubble Space Telescope* (*HST*). Complementing the pivotal research facilitated by *HST*’s deep observations of galaxy clusters (exemplified most recently by the Hubble Frontier Fields initiative; Lotz et al. 2016, and references therein), the observatory’s ability to acquire ‘snapshot’ images of a large number of objects, randomly selected from a large target pool, has proven uniquely efficient in surveying entire sub-populations of objects. The most impressive testimony to date of the power of SNAPshot observations of very X-ray luminous clusters is provided by our *HST* programmes GO-10491, -10875, -12166, and -12884, which imaged 86 clusters from the MACS sample, 28 of them in all of the four passbands chosen for this project (F606W, F814W, F110W, F140W). All proprietary rights were waived for these programmes, providing the scientific community with immediate access to all data.

In this paper we present and briefly explore several scientific applications of the MACS SNAPshot images, both to emphasize the wide range of astrophysical research topics one can address with these data and to stress their value for the selection of targets for detailed follow-up study. In keeping with these goals, our overview is not exhaustive, either in breadth or in depth: it does, however, aspire to convince the reader that SNAPshot surveys of massive galaxy clusters yield outstanding returns in terms of ‘science per exposure time.’

We structure this paper as follows: in Section 2 we describe the data and their reduction, and remind the reader of the cluster-

morphology classifications originally devised by Ebeling et al. (2007). In Section 3 we identify gravitational arcs produced by these powerful cluster lenses, before exploring, in Section 4, properties of the BCGs such as dust, signs of recent star formation, and their offset in colour from their host clusters’ red sequence. In Section 5 we then investigate the evolution of the cluster red sequence since $z \sim 0.5$, before, in Section 6, investigating the correlation between cluster X-ray luminosity and optical richness. In Section 7 we discuss the legacy value of this dataset and the release of the redshifts for all clusters in our sample. We present our conclusions in Section 8.

All magnitudes are measured and reported in the AB system (Oke & Gunn 1983); coordinates are quoted in the J2000.0 epoch. In our adopted concordance Λ CDM cosmology ($\Omega_m = 0.3$, $\Omega_\Lambda = 0.7$, and $h = 0.7$), one arcsecond on the sky corresponds to distances of 4.45 kpc and 5.76 kpc at $z = 0.3$ and $z = 0.45$, respectively.

2 OBSERVATIONS AND DATA ANALYSIS

2.1 Groundbased Imaging

As described in Ebeling et al. (2001), the MACS project used images in three optical passbands obtained with the University of Hawaii 2.2-m telescope to confirm the presence of galaxy overdensities at the location of X-ray selected cluster candidates. Cluster candidates that meet the MACS X-ray selection criteria but which lie too far south ($\delta < -40^\circ$) to be imaged in the optical from Maunakea were observed with facilities in the southern hemisphere. Due to the MACS team’s limited access to the required resources, this southern extension of MACS (dubbed ‘SMACS’) remains incomplete. An overview of the SMACS sample will be presented in a separate paper.

A brief overview of this imaging campaign also appears in Mann & Ebeling (2012) who use data from X-ray observations in conjunction with the aforementioned UH 2.2-m images to sort MACS clusters into morphological classes reflecting their apparent dynamical state. This classification system, introduced by Ebeling et al. (2007), assigns clusters to one of four classes ranging from the most relaxed (1) to the most disturbed (4), based on the system’s appearance in the X-ray and optical wavebands. Class-1 clusters feature a compact core and excellent alignment between the peak of the X-ray emission and the location of the cluster’s sole BCG; a Class-2 designation reflects reasonable X-ray/optical alignment and approximately concentric X-ray contours; Class 3 exhibits obvious small-scale structure and nonconcentric X-ray contours; and Class 4 systems show poor X-ray/optical alignment, multiple X-ray peaks, and no obvious BCG. Since not all of the clusters in this paper’s MACS subsample have X-ray data, we expand this classification scheme to also assign morphology classes using optical data alone¹. Aiming again to coarsely subdivide the range from fully relaxed to extremely disturbed, we base our optical classification on the symmetry of the cluster galaxy distribution and the degree to which it is dominated by a single bright galaxy. Similar to the scheme used in the X-ray-based classification, the morphological extremes are thus characterized by a single agglomeration of galaxies dominated by a single and central BCG (Class 1) and an association of several distinct subclusters featuring multiple

¹ For more sophisticated techniques and parameterisations see Wen & Han (2013) and references therein.

Table 1. Passbands and integration times

Instrument	Filter	Integration
ACS	F606W	1200 s
ACS	F814W	1440 s
WFC3	F110W	706 s
WFC3	F140W	706 s

BCGs of comparable brightness (Class 4). A comparison of optical and X-ray classifications performed independently by both authors found them to be well correlated and to differ by at most one class, with one exception². For seven SMACS clusters we forgo an optical morphology classification, since the availability of images in only one optical filter precludes a reliable discrimination between cluster galaxies and foreground objects.

2.2 Hubble Space Telescope

Our dataset consists of *HST* images of the 86 MACS and SMACS clusters (Table 8) imaged by the aforementioned *Hubble* SNAPshot programmes³. The integration times per cluster for each of the chosen four passbands appear in Table 1.

Note that, since the target list for these SNAPshot programmes excluded (by design) exceptional MACS clusters imaged previously with *HST* – such as the 12 MACS clusters at $z > 0.5$ (Ebeling et al. 2007) – the sample presented here is not representative of MACS as a whole. In addition, due to the opportunistic nature of the SNAPshot programme, many of our targets do not have images in all four passbands (Table 8 lists the passbands in which images were obtained for each cluster). Furthermore, images of a given target in different passbands are, in general, not aligned, since they were acquired at times and orientations dictated by *HST*’s scheduling requirements.

The work described here focuses largely on images acquired with the Advanced Camera for Surveys (ACS, Avila 2017) in the F606W and F814W bands. However, Table 8 also lists all near-infrared images obtained with the Wide-Field Camera 3 (WFC3, Dressel 2017) in the F110W and F140W passbands, where the lack of atmospheric absorption and emission puts space-based observatories at a huge advantage over groundbased telescopes (we note specific applications of our WFC3 data in Section 7).

Although one can derive various colours from combinations of passbands used by our SNAPshot programmes, we here focus on observations in the F606W and F814W filters, both to identify and parametrize the cluster red sequence (Section 5) and to screen BCGs for internal features. To this end, we *redrizzle*⁴ all images (where possible) to the F814W reference frame and pixel scales, and then run *SExtractor*⁵ (Bertin & Arnouts 1996) in dual-image mode, using F814W as the detection image. For clusters without an F814W image we use *SExtractor* in single-image mode on SNAPshots in other passbands – on the F606W image if available, otherwise on the F110W image; for these clusters we

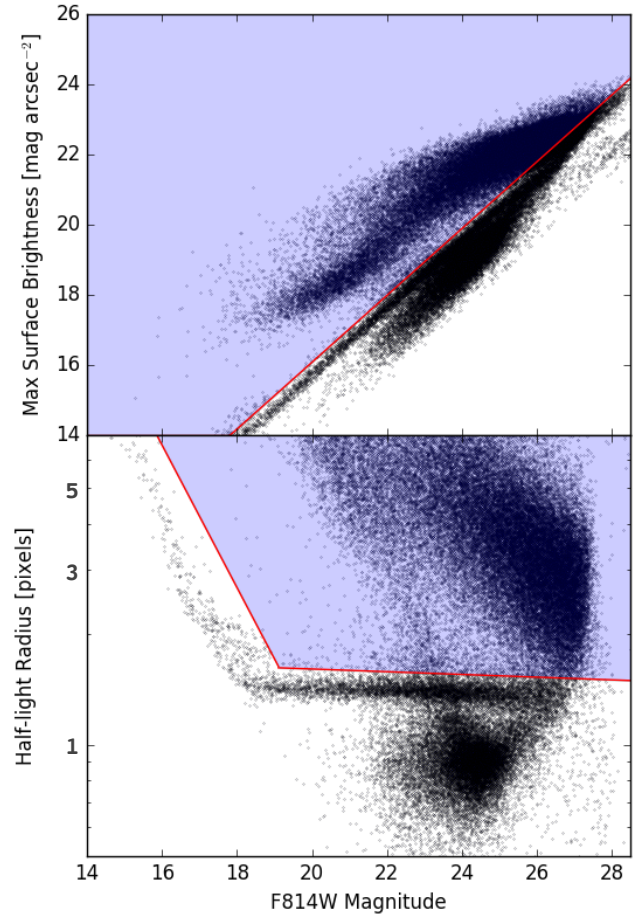


Figure 2. Star-galaxy separation based on surface brightness and half-light radius. The diagonal line of sources in the top panel and the (approximately) horizontal line of in the bottom panel correspond to the locus occupied by point sources (stars). We reject any source situated less than 2σ above this star line in either panel.

confine ourselves to identifying the BCGs and second-brightest red sequence members (G2) (see Section 4 and Table 8) with the help of colour information provided by groundbased images obtained during the compilation of the MACS sample (Ebeling et al. 2001). We express all photometry in terms of *SExtractor* isophote magnitudes.

In clusters with an F814W image, we then separate galaxies from stars and artefacts. As shown in Fig. 2, point sources (stars) occupy a well defined region (‘star line’) in the magnitude/surface brightness and magnitude/half-light radius planes. Any object on these lines is unresolved, and any detection below these lines is more compact than a point source and thus unphysical. We therefore select as galaxies only objects located at least 2σ above the star line in both panels.

The final two columns of Table 8 provide qualitative assessments of the cluster morphology in terms of relaxation state (see Section 2.1 for an overview).

3 GRAVITATIONAL LENSING

One of the primary motivations of our SNAPshot programme was to survey MACS clusters for signatures of strong gravitational lens-

² The lone exception is SMACS0234.7–5831. Its X-ray morphology indicates that it is a fully relaxed system, but a superimposed foreground group creates an optical appearance that led us (erroneously) to classify it as moderately disturbed.

³ GO-10491, GO-10875, GO-12166, GO-12884; PI Ebeling

⁴ using *DrizzlePac*: <http://drizzlepac.stsci.edu>

⁵ Version 2.19.5

ing in order to tentatively identify the most powerful cluster lenses. We here present a brief overview of the spectacular lensing features discovered in the course of this project; a discussion of some in-depth investigations enabled by our SNAP surveys appears in Section 7.

Figs. 3 and 4 show the most dramatic gravitational arcs produced by the gravity of our massive cluster targets. We separate this gallery into arcs detected by the automatic algorithm of Horesh et al. (2005) (Fig. 3), and other arcs (Fig. 4) that, although often just as impressive to the eye, were missed by our implementation of the algorithm due to low surface brightness, over-zealous deblending, or a low length-to-width ratio. The colour images in these figures use ‘true colour’ in the sense that the brightnesses of the RGB components are proportional to the specific intensities in the relevant filters. In addition, we display each image at the same dynamic stretch so that differences in image brightness consistently reflect actual differences in magnitude. Table 2 lists the coordinates of each of the arcs and the corresponding cluster lens. In the following we discuss in more detail the implementation and findings of automated arc-finding algorithms.

The main incentive for the development of arc-finding algorithms is the desire to efficiently and objectively compare the observed incidence of gravitational arcs with that predicted by numerical simulations of large-scale structure in various cosmologies. The results of such comparisons differ greatly: while the study of Bartelmann et al. (1998) finds the observed incidence to be orders of magnitude lower than the one predicted by their simulations for a Λ CDM cosmology, Zaritsky & Gonzalez (2003) and Gladders et al. (2003) report observed arc incidences that significantly exceed the very same predictions. Attempts to better understand these discrepancies considered the effects of cluster triaxiality (Oguri et al. 2003), source redshift (Dalal et al. 2004), and cluster mergers (Torri et al. 2004). Simulations by Meneghetti et al. (2010) predicted that strong lensing ability would correlate with X-ray luminosity and depend on cluster orientation; comparison with 12 MACS clusters (Meneghetti et al. 2011) still indicated a discrepancy between actual and observed lensing measures, but the discrepancy was much less than previous analytical models had predicted. (See also the review by Meneghetti et al. 2013.)

It was against this background that Horesh et al. (2005) developed an arc-finding algorithm in order to objectively compare the observed frequency of giant arcs with that of arcs produced by simulated clusters lensing real backgrounds. The ensuing study led them to conclude that the observed and simulated arc incidences are in fact consistent. (See also Horesh et al. 2011 for a similar study using the Millennium Simulation.) Using their algorithm to detect giant arcs in *HST* imaging data, Horesh et al. (2010) find that X-ray selected clusters (their sample overlaps with ours) give rise to 6–8 times more giant arcs per cluster than those from the optically selected comparison sample, suggesting a difference in cluster mass of an order of magnitude.

While Horesh et al.’s code is no longer publicly available, we attempt to reconstruct it from the published description in order to quantify the arc production of our cluster sample. We note that the algorithm is sensitive to the background-estimation procedure as well as to various parameter settings in the data-reduction pipelines. These differences can affect the inclusion of marginal pixels in an arc, resulting in slightly different length-width ratios; in some cases, the arc will be split into two or more pieces, neither of which passes the length-to-width threshold. While our results are thus not directly comparable with those of Horesh et al. (2010) (even where their cluster sample overlaps ours), the algorithm pro-

Arc	Host Cluster	Right Ascension	Declination
1	MACSJ0242.5–2132	02:42:37.32	–21:32:20.6
2	MACSJ0257.6–2209	02:57:39.01	–22:09:26.0
3	MACSJ0451.9+0006	04:51:53.44	+00:06:41.5
4	MACSJ0451.9+0006	04:51:57.13	+00:06:16.0
5	MACSJ0520.7–1328	05:20:40.33	–13:28:28.6
6	MACSJ0712.3+5931	07:12:17.60	+59:32:16.2
7	MACSJ1105.7–1015	11:05:47.54	–10:15:07.7
8	MACSJ1115.2+5320	11:15:17.55	+53:19:04.4
9	MACSJ1115.2+5320	11:15:18.26	+53:19:49.5
10	MACSJ1133.2+5008	11:33:14.20	+50:08:39.2
11	MACSJ1206.2–0847	12:06:10.74	–08:48:04.1
12	MACSJ1354.6+7715	13:54:09.67	+77:15:56.9
13	MACSJ1354.6+7715	13:54:24.47	+77:15:30.3
14	MACSJ1354.6+7715	13:54:41.98	+77:15:24.9
15	MACSJ1526.7+1647	15:26:45.11	+16:47:45.5
16	MACSJ1738.1+6006	17:38:08.04	+60:06:09.0
17	MACSJ2051.1+0215	20:51:09.91	+02:16:16.6
18	MACSJ2135.2–0102	21:35:10.57	–01:02:30.1
19	SMACSJ0549.3–6205	05:49:12.54	–62:06:18.4
20	SMACSJ2031.8–4036	20:31:46.22	–40:37:06.0
21	MACSJ0032.1+1808	00:32:12.10	+18:07:53.4
22	MACSJ0034.4+0225	00:34:27.36	+02:25:18.2
23	MACSJ0140.0–0555	01:40:01.47	–05:55:09.7
24	MACSJ0152.5–2852	01:52:34.75	–28:53:51.8
25	MACSJ0308.9+2645	03:08:56.31	+26:45:06.3
26	MACSJ0520.7–1328	05:20:41.96	–13:28:34.7
27	MACSJ0947.2+7623	09:47:08.18	+76:23:24.1
28	MACSJ0947.2+7623	09:47:15.13	+76:23:03.0
29	MACSJ1142.4+5831	11:42:22.70	+58:31:31.7
30	MACSJ1142.4+5831	11:42:24.75	+58:31:16.4
31	MACSJ1142.4+5831	11:42:26.35	+58:32:53.4
32	MACSJ1142.4+5831	11:42:26.98	+58:30:47.3
33	MACSJ1206.2–0847	12:06:11.26	–08:47:43.7
34	MACSJ1319.9+7003	13:20:06.03	+70:04:26.7
35	MACSJ1354.6+7715	13:54:08.75	+77:15:50.5
36	MACSJ1452.9+5802	14:52:50.37	+58:01:35.7
37	MACSJ2135.2–0102	21:35:11.81	–01:03:35.3
38	MACSJ2135.2–0102	21:35:12.70	–01:01:44.0
39	MACSJ2149.3+0951	21:49:20.06	+09:51:26.1
40	SMACSJ0234.7–5831	02:34:39.09	–58:31:36.5

Table 2. Host clusters and coordinates for the gravitational arcs shown in Figs. 3 and 4. Arc numbers correspond to the labels in the upper left corners of the images in the figures. Arcs 1–20 were detected by our implementation of Horesh et al. (2005)’s algorithm, whereas arcs 21–40 were not.

vides a simple means of investigating whether lensing efficiency evolves with redshift.

Sorting the clusters into redshift bins [0.3, 0.4) and [0.4, 0.5), we obtain the arc-production efficiencies (arcs per cluster) shown in Fig. 5. In agreement with the findings of Horesh et al. (2010), more distant clusters tend to produce more arcs than nearer clusters, but the trend is not statistically significant within the redshift range probed by MACS. Note that our results are not in conflict with those of Xu et al. (2016) who, using a more robust (and not publicly available) arc-finding algorithm, examine the lensing efficiency of clusters observed by the CLASH programme and find a slight – but again statistically insignificant – decrease of lensing efficiency with redshift⁶. Since lensing efficiency correlates with cluster mass, selection biases are bound to result in mild increases

⁶ Note that Xu et al. (2016) find lensing efficiencies over four times greater

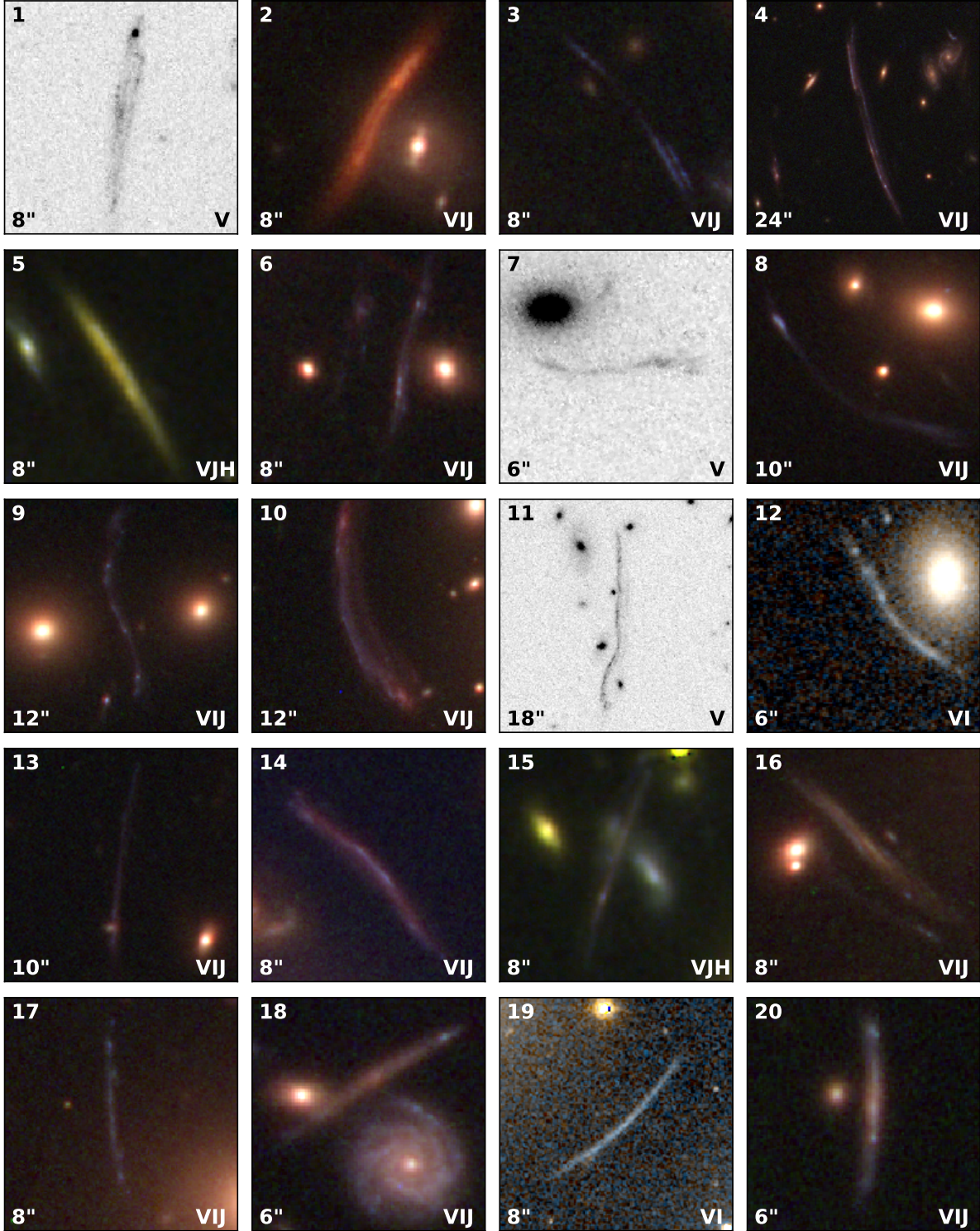


Figure 3. A sample of the arcs identified by the algorithm of Horesh et al. (2005). Each colour image is ‘true colour’ in that the RGB brightnesses correspond to the specific intensities in the bandpasses used in constructing the image. All images utilize the same intensity stretch in order to communicate the range of brightnesses of these arcs. Note that all images do not represent the same solid angle on the sky; instead, the notation at the lower left of each image specifies the length (in arcseconds) of one side of the square. The coordinates (and lensing clusters) of each arc appear in Table 2, indexed by the numbers at the upper left of each image. The letters at the lower right of each image specify the photometric bands approximating the *HST* filters used in constructing the image: $V = F606W$; $I = F814W$; $J = F110W$; $H = F140W$. Where three filters appear, they correspond to the blue, green, and red components, respectively, of the image. Where only two filters appear, they correspond to the blue and red components (respectively), the green component being the average of the intensity in the two filters. North is up, west is right.

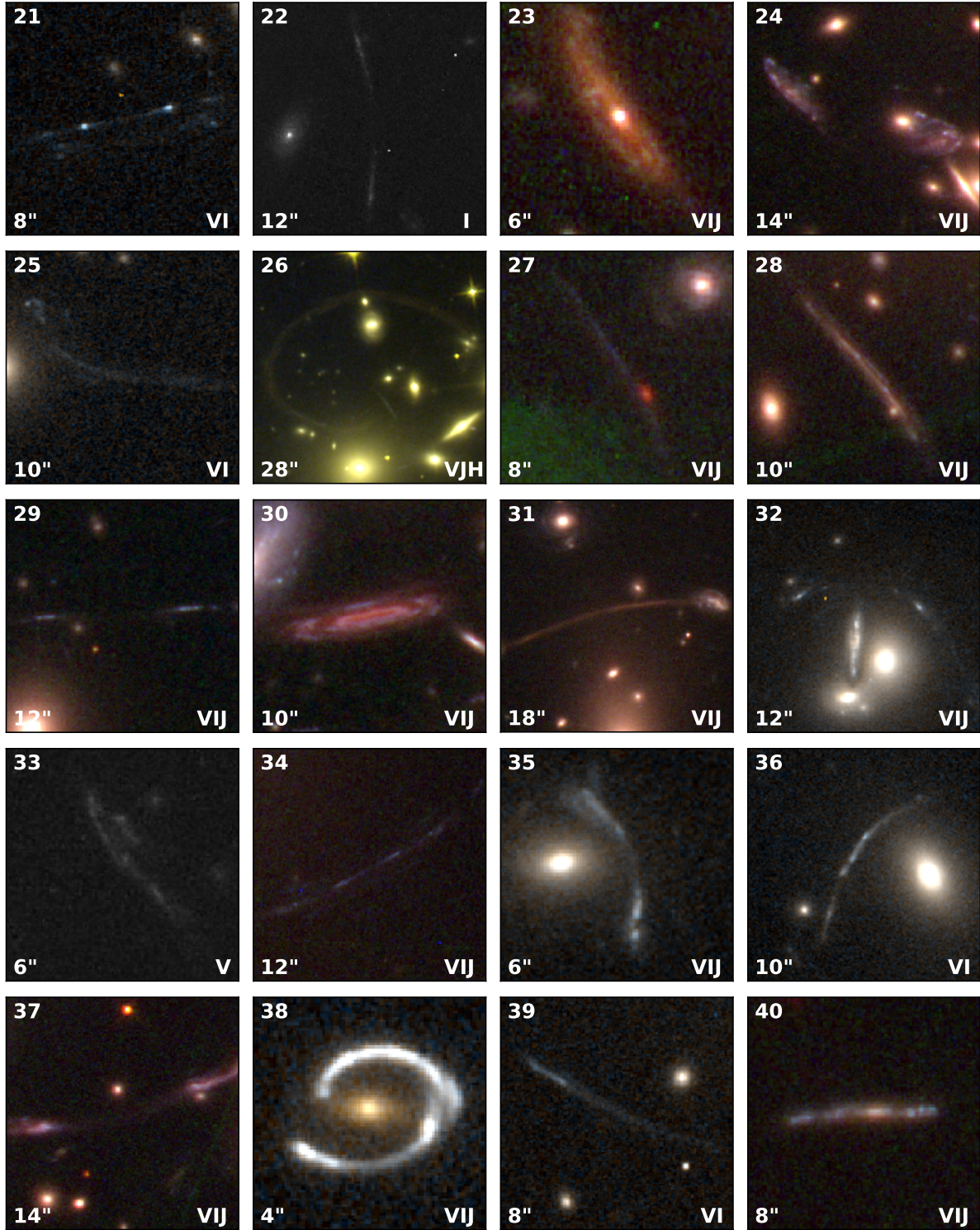


Figure 4. A sample of the arcs *not* detected by our implementation of the algorithm of Horesh et al. (2005). See caption of Fig. 3 for explanation of colour and stretch. The side length of each image appears at its lower left corner, and the letters at the lower right specify the photometric bands approximating the *HST* filters used in constructing the image: $V = F606W$; $I = F814W$; $J = F110W$; $H = F140W$. The coordinates and host cluster of each arc appear in Table 2, indexed by the numbers at the upper left of the image. North is up, west is right.

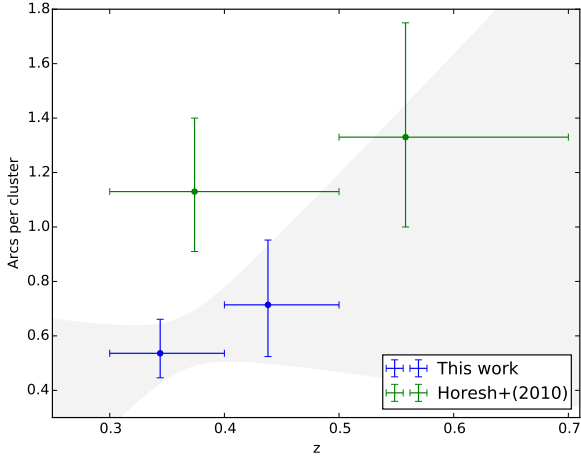


Figure 5. Arc-production efficiency of 77 MACS clusters, defined as the number of giant arcs ($\ell/w \geq 8$) detected by Horesh et al. (2005)’s algorithm divided by the number of clusters in the redshift bin. Vertical error bars indicate 68 per cent Poisson confidence intervals, and horizontal error bars indicate bin widths; data points appear at the mean redshift of the clusters in a given bin. We also show the results from Horesh et al. (2010)’s analysis. Note that one cannot directly compare the two sets of results due to the sensitivity of the algorithm to differences in the background estimation and the image-processing pipelines. The shaded area marks the 1σ error region for a linear fit to our two data points. Neither our data nor those of Horesh et al. (2010) rule out a redshift-independent arc-production efficiency.

of the lensing efficiency with redshift for flux-limited cluster samples such as MACS (more distant clusters tend to be more massive) and may well create the opposite trend in samples without quantifiable selection criteria such as the one compiled for CLASH.

4 BCG PROPERTIES

Although identifying powerful cluster lenses was the primary goal of our SNAPshot surveys, characterizing (at high angular resolution) the galaxy population of the cluster lenses themselves was an important secondary aim. Of particular interest in these contexts are two special classes of cluster members: galaxies observed in the process of being accreted by the cluster (either from the surrounding field or during a cluster merger), and (at the opposite end of the evolution spectrum) the giant ellipticals in the cluster centres, the BCGs. Insights into the properties of the former class of galaxies (often dubbed ‘jellyfish’ galaxies) from our SNAPshot observations appear in Ebeling et al. (2014), McPartland et al. (2016), and Ebeling et al. 2018 (in preparation). We therefore focus here on the properties of MACS BCGs as viewed in *HST* SNAPshots.

We use *HST* photometry and colours, i.e., `SExtractor`-derived magnitudes, to identify the BCG as well as the second-brightest cluster galaxy (G2) for each cluster in our sample. We resort to groundbased imaging (see Section 2.1) where colour information is not available from *HST* and also routinely scrutinize our $7' \times 7'$ groundbased images to ensure that no brighter cluster member is present outside the field of view of our *HST* images. We

note that all BCGs thus identified have been spectroscopically confirmed as cluster members. For seven SMACS clusters for which neither ground- nor space-based colour information is readily available, our BCG identifications should be considered tentative; we also do not identify G2. Table 8 lists our BCG and G2 magnitudes and coordinates as well as the passband in which the magnitude is calculated (F814W where available; F606W next in preference; and F110W if neither ACS band is available).

4.1 BCG morphology

In an approach similar to that in Section 3, we present a gallery of BCG images, as obtained by our SNAPshot programmes, in Fig. 6 (F606W/F814W) and Fig. 7 (various filters); all images span 40 kpc per side at the respective cluster redshift. As in Figs. 3 and 4, the images in Fig. 6 and Fig. 7 are shown at uniform stretch and contrast; the smaller inset images, however, use display parameters that have been adjusted to emphasize faint structural features in the very cores of these systems. Our gallery does not show all BCGs but only those that exhibit deviations from a regular, smooth surface brightness distribution. In both figures we highlight features of interest, such as central point sources, multiple nuclei, shells, unusually low surface brightness, compact (but not pointlike) cores, and irregular structure (most commonly caused by dust lanes or star bursts). We also mark a few BCGs as featuring satellite galaxies, but we note that the underlying apparent overdensity of galaxies near the BCG could be simply a projection effect.

We draw particular attention to extreme examples of pronounced and irregular structure indicative of active star formation; these include the BCGs of MACSJ0159.8–0849, MACSJ0242.5–2132, MACSJ0547.0–3904, MACSJ0913.7+4056, MACSJ0947.2+7623 (aka RBS797; Schindler et al. 2001), MACSJ1133.2+5008, MACSJ1354.6+7715, MACSJ1447.4+0827, and SMACSJ0549.3–6205. Also worth mentioning are the unusual, faint, central depressions in the surface brightness of the BCGs of MACSJ0257.7–2209 and MACSJ1006.9+3200, only visible at the custom stretch of the respective inset images in Figs. 6 and 7; these are similar to features highlighted by Laine et al. (2003) in their study of *HST* images of BCGs in nearby clusters ($z < 0.06$). We consider the possibility that these features might be the result of a dynamical process like core scouring (see, e.g., Begelman et al. 1980; Thomas et al. 2014), in which mergers produce a (temporarily) binary black hole that ejects stars from the core. However, for both of these BCGs the luminosity decrease in the dark spot weakens in redder passbands, suggesting that the cause of the depression is extinction by dust clouds or rings. We thus speculate that MACSJ0257.7–2209 and MACSJ1006.9+3200 might be high-redshift equivalents of NGC3311, the BCG of A1060 (Laine et al. 2003). A more quantitative comparison with the data and classifications presented by Laine et al. (2003) is clearly warranted in view of the similarity of the features identified as dust rings, dust spirals, and circumnuclear disks in their work.

Overall, 14 out of 47 clusters with *HST* SNAPshot images in both ACS filters (F606W and F814W) exhibit evidence of various types of activity, including cannibalism, star-formation, and dust, underlining yet again that, in the cores of massive clusters, giant ellipticals can be far from ‘red and dead.’

4.2 Colour offsets and BCG dominance

In spite of its dominant position among cluster members, the BCG does not always lie on the cluster red sequence. Both a steeper Ko-

than ours, an impact of using both a different algorithm and a less restrictive ℓ/w criterion.



Figure 6. Cut-outs (40 kpc each side) of BCGs showing various features of interest. All images use F110W, F814W, and F606W data for the r, g, and b channel, respectively. The code(s) in the lower left corner indicate(s) the presence of the following, as determined visually: B – low surface brightness; C – compact core; L – layers/shells; N – multiple nuclei; P – point source; S/W – strong/weak structure; Sa – satellite galaxies. Main images displayed with equal brightness stretch. Insets display the central 10 kpc at a different brightness to show detail. North is up, and west is right.

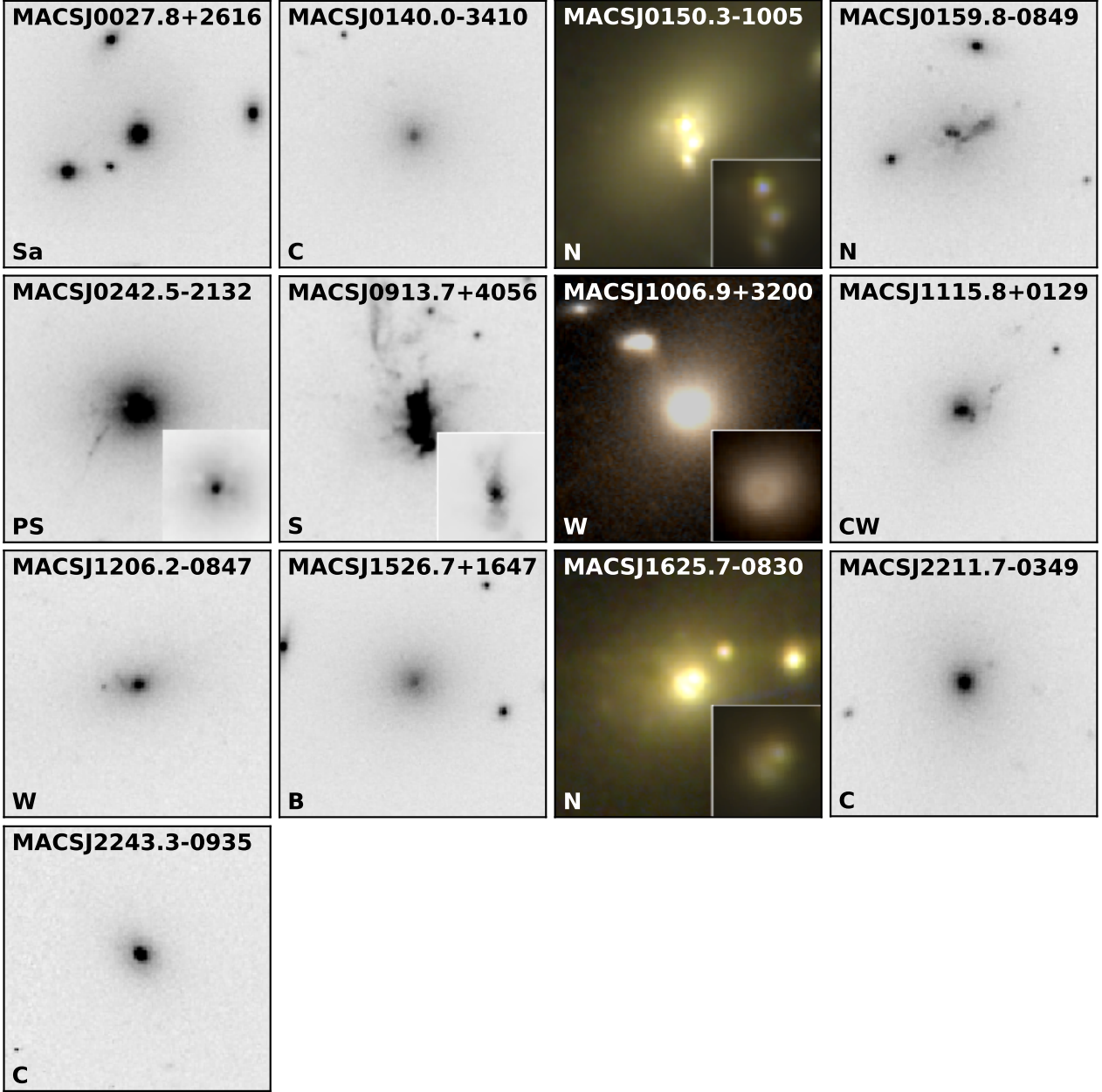


Figure 7. Cut-outs (40 kpc each side) of BCGs showing various features of interest. The code(s) in the lower left corner indicate(s) the presence of the following, as determined visually: B – low surface brightness; C – compact core; N – multiple nuclei; P – point source; S/W – strong/weak structure; Sa – satellite galaxies. Main images displayed with equal brightness stretch. Insets display the central 10 kpc at a different brightness to show detail. Monochrome images are from F606W; for MACSJ1006.9+3200, red is from F814W, blue is from F606W, and green is from the average of the two; for the remaining two images, red is from F140W, green from F110W, and blue from F814W. North is up, and west is right.

rmendy relation (Bildfell et al. 2008) and evidence of recent star formation in the BCGs of cool-core clusters (e.g., Johnstone et al. 1987; Edge 2001; Edwards et al. 2007) suggest a different assembly history for these galaxies compared to that of other cluster ellipticals. Bildfell et al. (2008)’s analysis of the Canadian Cluster Comparison Project finds that about 25 per cent of the clusters host BCGs offset from their cluster’s red sequence by 0.5 to 1.0 magnitudes in $(g' - r')$. In the following we explore whether similar offsets are present in the BCGs of our target clusters and, if so, how such colour offsets correlate with other BCG or host cluster properties.

As noted earlier (see Table 3), our SNAPs sample contains 47 clusters for which we can define the red sequence. From this set we exclude MACSJ0947.2+7623 because its BCG colour is suspect, due to an internal telescope reflection in the F814W image that extends into the BCG. For the remaining 46 clusters, we compute the colour offset of the BCG in units of the Gaussian width of the respective red sequence. We find several noticeably blue outliers; these appear in Fig. 8, which normalizes the offset by the red sequence width. If we consider absolute colour offsets, only the most extreme offset (from MACSJ1447.4+0827, with $\Delta\text{mag} = -0.46$) approaches the size of those noted by Bildfell et al. (2008); the

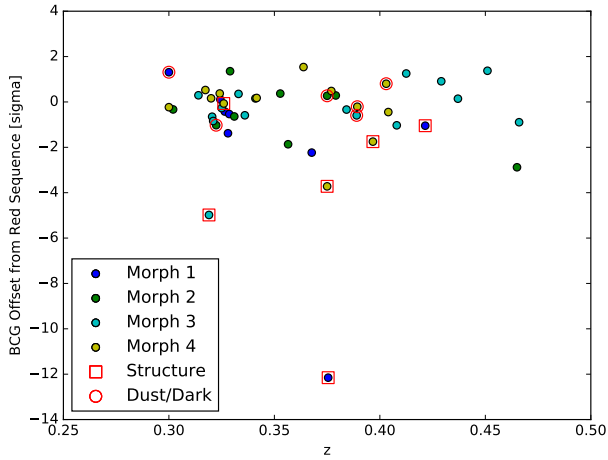


Figure 8. Colour offset (from the red sequence) of BCGs for 46 MACS clusters, in units of the 1σ red-sequence width, with morphology class as noted in the legend. BCGs with noted structural features (see Figs. 6, 7) are marked. The largest offsets belong to the BCGs of MACSJ1447.4+0827 (-12σ), MACSJ0547.0–3904 (-5.0σ), and SMACSJ0549.3–6205 (-3.7σ). Although the BCG of MACSJ0947.2+7623 does not appear in this figure due to contamination of its F814W image, it would most likely be a fourth extreme outlier.

two next largest colour offsets (from SMACSJ0549.3–6205 and MACSJ0547.0–3904) are -0.15 and -0.14 , respectively. We attribute this difference to a disparity in the colours used to define the red sequence: unlike our F606W and F814W passbands (at our clusters’ median redshift of $z = 0.36$), Bildfell and collaborators’ g' and r' filters almost perfectly straddle the 4000\AA break (at their typical redshift of $z \sim 0.25$); hence, their $g' - r'$ colours will be more sensitive to ongoing star formation. Considering the observed colour offsets in terms of 1σ red-sequence width, we find that 4 out of 46 BCGs (9 per cent) fall more than 2.5σ below the red sequence. Green et al. (2016), using a somewhat different methodology, observe a similar fraction of BCGs to be offset in $g - r$.

While the BCG colour offset exhibits no obvious evolution with redshift (see Fig. 8), it clearly correlates with the presence of observable structure in the BCG. Only three BCGs feature offsets in excess of -3σ (MACSJ0547.0–3904, SMACSJ0549.3–6205, and MACSJ1447.4+0827), and each of them displays significant internal structure in the form of striking blue filaments and apparent knots of star formation (see Figs. 8 and 6). The BCG of MACSJ0547.0–3904 also exhibits a point-like core in our SNAP-shot images, which coincides with an X-ray point source in our *Chandra* image of the cluster and thus strongly suggests nuclear activity. In addition to these extreme examples, nine other BCGs (marked in Fig. 8 and shown in Fig. 6) are not significantly offset from the red sequence but nonetheless show internal structure, dust lanes, and/or dark spots, including the aforementioned BCGs of MACSJ0257.7–2209 and MACSJ1006.9+3200. Finally, MACSJ0308.9+2645 exhibits multiple galaxies near or within the halo of its BCG, suggesting either an extreme case of projection or unrelated cluster members, or imminent galactic cannibalism.

Finally, we explore trends in the BCG dominance (defined as the magnitude difference between the BCG and the second-brightest cluster galaxy). No correlation with redshift is observed, either for the full sample or for any subset when split according to

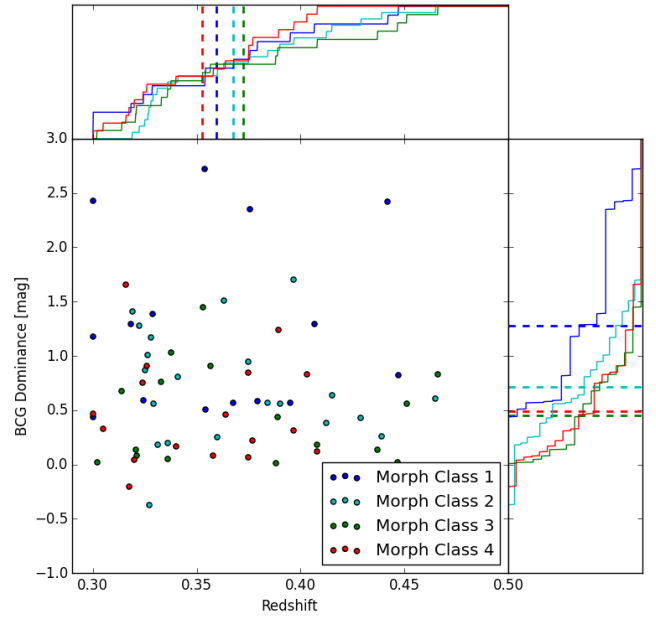


Figure 9. BCG dominance as a function of redshift for the four cluster morphology classes described in Section 2. For each of the four morphology classes, the cumulative distribution functions of redshift and BCG dominance, as well as the corresponding mean values (dotted lines), appear in the top and right panels, respectively.

the relaxation state of the host cluster, as measured by morphology class (Fig. 9). Neither the cumulative redshift distribution functions nor the mean redshifts for the four morphology classes (top panel of Fig. 9) show any sign of progression from disturbed to relaxed (or vice versa); applying two-sided Kolmogorov-Smirnov tests to the redshift distributions of the various morphology classes, one finds the largest difference between classes 2 and 4 ($D = 0.27$), which is, however, insignificant ($p = 0.44$). Clear differences, however, are observed for the degree of BCG dominance between different morphology classes (e.g., $D = 0.58$ for classes 1 and 4, corresponding to $p = 0.005$); this outcome is unsurprising given that BCG dominance is one criterion for determining cluster morphology. In addition, the roughly equal number of clusters in each morphology class demonstrates that the frequency of and timescale for cluster mergers is at most of the same order of magnitude as the cosmic time probed by this survey.

5 EVOLUTION OF THE RED-SEQUENCE SLOPE

Elliptical galaxies in clusters tend to form a tight ‘red sequence’ in colour-magnitude space (Fig. 10). Tentative red sequences have been observed in clusters (or proto-clusters) at redshifts as high as $z \sim 2$ (e.g., Tanaka et al. 2010; Spitler et al. 2012; Andreon et al. 2014).

The red sequence has been interpreted as a mass-metallicity relation, in the sense that bright, massive galaxies lose fewer of their metals to the intergalactic medium (Kodama & Arimoto 1997); in this scenario, variations in stellar age would be the source of scatter along the sequence (Bower et al. 1992; Jaffé et al. 2011). Other authors (De Lucia et al. 2007; Smith et al. 2008; Stott et al.

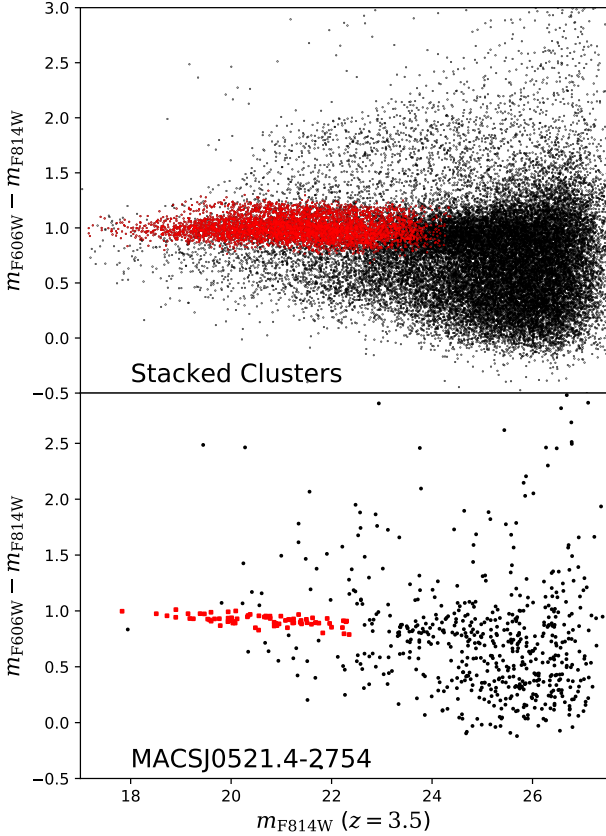


Figure 10. Colour-magnitude diagram based on F606W and F814W magnitudes illustrating the red sequence – both for the stack of all clusters (top panel), and for one arbitrarily chosen cluster (MACSJ0521.4–2754, bottom panel). For the top panel, the F814W magnitudes have been K -corrected to a redshift of 0.35. Black points show galaxies in the ACS field of view; red squares show presumed cluster members, defined by an offset of less than 3σ from the red sequence for this cluster. Note (in the top panel) that the width of the stacked red sequence is inflated by variations in galactic extinction and reddening, with the most extreme cases appearing almost fully above the main red-sequence band.

2009) propose an age contribution to the red-sequence slope. In this scenario, faint galaxies migrate to the red sequence as they fall into the cluster and are quenched by interaction with intracluster gas; these recently quenched galaxies are at first bluer than the older, brighter cluster members, but by the same token they redden more rapidly. Hence, the red sequence slope would in this scenario flatten over time, i.e., would be more negative at higher redshift.

The observed slope does indeed evolve with redshift (López-Cruz 1997; Gladders et al. 1998; López-Cruz et al. 2004); however, some – and perhaps all – of this evolution is the result of K correction. In order to isolate any physical evolution, whether caused by a changing mass-metallicity relation or by an age contribution, we must thus transform the slopes to the cluster rest frame.

Since our SNAPshot sample includes 47 clusters with both

F814W and F606W coverage (see Table 3), we use these clusters to investigate the evolution of the red-sequence slope, in these colours, from $z = 0.3$ to 0.5 . We establish linear fits to the red sequence for each cluster iteratively down to a limit that is four magnitudes fainter than the mean of the second- and third-brightest cluster members. For a meaningful interpretation of the observed evolution of the slope, we must disentangle the effects of K corrections from any intrinsic evolution of cluster or galaxy properties (e.g., in metallicity or stellar age). We thus transform the observed F606W–F814W slope to a rest-frame $U - V$ slope using the prescription from Appendix B of Mei et al. (2009), also employed by Cerulo et al. (2016). This approach uses 42 synthetic stellar population models from the Bruzual & Charlot (2003) collection. These models include 7 formation redshifts (spaced evenly from $z = 2$ to 5), three metallicities ($0.4Z_{\odot}$, Z_{\odot} , and $2.5Z_{\odot}$), and two star formation histories (instantaneous burst, and exponentially declining star formation with 1-Gyr e -folding). For cluster redshifts ranging from $z = 0.2$ to 0.6 we calculate the rest-frame $U - V$ colours and the observer-frame F606W–F814W colours for each model and then determine the best-fit linear relationship

$$C_{UV,rf} = A(z) + B(z) \cdot C_{ACS,obs},$$

where $C_{ACS,obs}$ denotes F606W–F814W colour. We thus obtain the colour conversion factors $A(z)$ and $B(z)$ as functions of redshift.

The red-sequence slopes m (and their uncertainties σ_m) in rest-frame and ACS colours are then related as follows:

$$\begin{aligned} m_{rf} &= B(z) \cdot m_{ACS}, \\ \sigma_{m,rf} &= B(z) \cdot \sigma_{m,ACS}. \end{aligned}$$

Converting the observed slopes into rest-frame $U - V$ slopes using this prescription, we find only weak intrinsic evolution that is in fact consistent with (i.e., differing by only two sigma from) no evolution for the $0.3 \leq z \leq 0.5$ range (Fig. 11).

Stott et al. (2009) analyse red-sequence slopes using the Coma cluster, a set of LARCS clusters (Las Campanas/AAT Rich Cluster Survey; Pimbblet et al. 2001, 2006) at $z \sim 0.1$, and a set of MACS clusters at $z \sim 0.5$. (Stott et al. 2009’s set of MACS clusters partially overlaps ours.) They find significant evolution of the rest-frame slope with redshift, roughly consistent with (though lower than) our best-fit line shown in Fig. 11. However, unlike theirs, our results are consistent with no evolution. These disparate results highlight the difficulty of comparing red-sequence slopes from different studies; challenges include not only intrinsic statistical scatter in the results but also systematic differences in fitting algorithms, photometric techniques, and parameter definitions. Acknowledging this caveat, we plot our results alongside those of Stott et al. (2009) in Fig. 12 and also show observational data from the corresponding plot of Cerulo et al. (2016)’s fig. 4.

We note that our conclusion of weak or no evolution of the red-sequence slope is consistent with the general pattern of the data out to $z \sim 1.5$. By themselves, however, the data out to $z \sim 0.7$ suggest a weak flattening of the slope over time. Although the large uncertainties of corresponding results for individual high-redshift clusters limit their power to constrain any evolution, the data at $z > 0.7$ suggest that a red sequence was already in place in clusters as distant as $z \sim 1.5$, and that the evolution of the red-sequence slope since that time was modest at best. Furthermore, we note the success of photometric redshift estimators that assume passive evolution of the red sequence following a high-redshift burst of star formation (Song et al. 2012; Bleem et al. 2015; Planck Collaboration et al. 2015); the typical error of these estimators is only a

Name Red Sequence BCG	
	Slope (b)	Zero-point (a)	half-width (σ)	m_{606}	m_{814}
MACSJ0011.7–1523	-0.027 ± 0.004	1.003 ± 0.080	0.042 ± 0.004	19.49	18.40
MACSJ0032.1+1808	-0.026 ± 0.003	1.114 ± 0.064	0.039 ± 0.004	19.70	18.50
MACSJ0035.4–2015	-0.027 ± 0.004	0.992 ± 0.088	0.036 ± 0.004	18.92	17.82
MACSJ0110.1+3211	-0.023 ± 0.004	0.983 ± 0.081	0.025 ± 0.003	19.09	18.04
MACSJ0140.0–0555	-0.025 ± 0.005	1.144 ± 0.109	0.024 ± 0.003	19.68	18.44
MACSJ0152.5–2852	-0.029 ± 0.003	1.046 ± 0.066	0.035 ± 0.003	20.09	18.93
MACSJ0257.6–2209	-0.023 ± 0.004	0.934 ± 0.081	0.033 ± 0.004	17.80	16.81
MACSJ0308.9+2645	-0.028 ± 0.004	1.186 ± 0.078	0.038 ± 0.004	19.09	17.89
MACSJ0451.9+0006	-0.027 ± 0.004	1.113 ± 0.091	0.033 ± 0.003	19.72	18.51
MACSJ0521.4–2754	-0.025 ± 0.006	0.908 ± 0.120	0.036 ± 0.005	18.83	17.83
MACSJ0547.0–3904	-0.025 ± 0.007	0.949 ± 0.157	0.029 ± 0.005	18.57	17.68
MACSJ0712.3+5931	-0.021 ± 0.004	0.970 ± 0.096	0.026 ± 0.004	18.53	17.51
MACSJ0845.4+0327	-0.018 ± 0.004	0.955 ± 0.085	0.037 ± 0.004	18.85	17.79
MACSJ0916.1–0023	-0.032 ± 0.005	0.885 ± 0.112	0.053 ± 0.004	18.89	17.90
MACSJ0947.2+7623	-0.036 ± 0.003	1.024 ± 0.068	0.008 ± 0.004	18.36	17.01
MACSJ0949.8+1708	-0.025 ± 0.003	1.014 ± 0.061	0.022 ± 0.003	19.16	18.09
MACSJ1006.9+3200	-0.025 ± 0.005	1.008 ± 0.116	0.047 ± 0.004	18.90	17.77
MACSJ1115.2+5320	-0.042 ± 0.004	1.123 ± 0.095	0.044 ± 0.004	19.31	18.10
MACSJ1124.5+4351	-0.023 ± 0.004	0.988 ± 0.092	0.026 ± 0.003	19.72	18.74
MACSJ1133.2+5008	-0.001 ± 0.009	1.003 ± 0.201	0.043 ± 0.007	19.13	18.09
MACSJ1142.4+5831	-0.016 ± 0.004	0.904 ± 0.080	0.038 ± 0.004	17.66	16.69
MACSJ1226.8+2153C	-0.034 ± 0.005	1.072 ± 0.119	0.032 ± 0.005	19.90	18.74
MACSJ1236.9+6311	-0.024 ± 0.004	0.878 ± 0.081	0.028 ± 0.003	18.49	17.54
MACSJ1258.0+4702	-0.023 ± 0.007	0.952 ± 0.149	0.029 ± 0.004	19.15	18.15
MACSJ1319.9+7003	-0.028 ± 0.004	0.911 ± 0.095	0.035 ± 0.005	18.34	17.34
MACSJ1328.2+5244	-0.030 ± 0.005	0.895 ± 0.100	0.035 ± 0.004	18.81	17.84
MACSJ1354.6+7715	-0.020 ± 0.003	1.036 ± 0.070	0.025 ± 0.001	19.14	18.09
MACSJ1447.4+0827	-0.042 ± 0.005	1.018 ± 0.112	0.037 ± 0.005	17.75	17.02
MACSJ1452.9+5802	-0.021 ± 0.003	0.910 ± 0.064	0.029 ± 0.003	18.68	17.69
MACSJ1621.3+3810	-0.029 ± 0.006	1.146 ± 0.121	0.036 ± 0.004	19.90	18.79
MACSJ1644.9+0139	-0.030 ± 0.004	1.003 ± 0.087	0.036 ± 0.004	18.97	17.89
MACSJ1652.3+5534	-0.017 ± 0.006	0.922 ± 0.117	0.041 ± 0.006	18.67	17.69
MACSJ1731.6+2252	-0.022 ± 0.004	1.038 ± 0.083	0.035 ± 0.003	18.41	17.30
MACSJ1738.1+6006	-0.028 ± 0.003	0.976 ± 0.075	0.034 ± 0.003	18.83	17.78
MACSJ1752.0+4440	-0.015 ± 0.005	0.954 ± 0.103	0.045 ± 0.005	19.49	18.43
MACSJ1806.8+2931	-0.017 ± 0.005	0.930 ± 0.113	0.034 ± 0.004	19.06	18.03
MACSJ2050.7+0123	-0.023 ± 0.006	1.002 ± 0.138	0.053 ± 0.008	18.80	17.70
MACSJ2051.1+0215	-0.034 ± 0.004	1.013 ± 0.083	0.032 ± 0.004	18.72	17.62
MACSJ2135.2–0102	-0.019 ± 0.004	0.960 ± 0.080	0.018 ± 0.002	18.46	17.43
MACSJ2149.3+0951	-0.006 ± 0.009	1.031 ± 0.183	0.050 ± 0.011	19.42	18.36
MACSJ2241.8+1732	-0.018 ± 0.003	0.918 ± 0.060	0.027 ± 0.003	18.86	17.87
SMACSJ0234.7–5831	-0.033 ± 0.005	1.054 ± 0.110	0.038 ± 0.005	19.87	18.78
SMACSJ0549.3–6205	-0.033 ± 0.005	1.013 ± 0.106	0.039 ± 0.004	18.87	17.90
SMACSJ0600.2–4353	-0.020 ± 0.005	0.952 ± 0.101	0.032 ± 0.004	18.29	17.27
SMACSJ0723.3–7327	-0.030 ± 0.005	1.171 ± 0.108	0.052 ± 0.005	20.35	19.14
SMACSJ2031.8–4036	-0.021 ± 0.004	0.965 ± 0.079	0.030 ± 0.003	18.81	17.77
SMACSJ2131.1–4019	-0.033 ± 0.008	1.107 ± 0.162	0.045 ± 0.005	19.25	18.10

Table 3. Red sequence and BCG colour information. The red sequence is defined in the space ($m_{F606W} - m_{F814W}$) vs. m_{F814W} , with functional form $C_{RS} = a + b \times (m_{F814W} - 21.0)$. Magnitude uncertainties $\lesssim .01$.

few per cent. Acknowledging the aforementioned caveats, we thus conclude that a strong age contribution to the evolution of the red-sequence slope in massive clusters is not favoured by the existing data.

6 X-RAY PROPERTIES

High-resolution X-ray data have been obtained with *Chandra* for 45 clusters in our sample. Table 4 lists the point-source-corrected X-ray luminosity L_X for the 0.01–2.4 keV band; it also lists the

position of the peak of the X-ray surface brightness, measured after adaptive smoothing using the ASMOOTH algorithm (Ebeling et al. 2006). While a full analysis of the available X-ray data is far beyond the scope of this paper, we use the mentioned X-ray characteristics to explore two correlations with optical cluster properties derived from our SNAPshot data: the L_X -richness relation and the X-ray/optical alignment of our cluster targets.

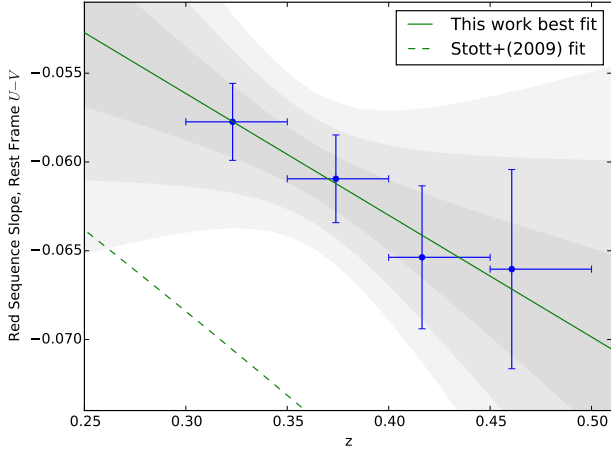


Figure 11. Red-sequence slope (rest-frame $U - V$) for 47 MACS clusters as a function of redshift. Horizontal error bars represent the bin widths ($\Delta z = 0.05$), and the horizontal placement of the data points shows the mean redshifts of the clusters in each bin. The solid green line shows the best-fit linear expression for the evolution of the slope; grey contours show the 1σ -, 2σ - and 3σ -confidence regions for the fit. Note that our fit differs by only 2σ from a finding of no evolution. The dashed line shows the fit of Stott et al. (2009) – see their data plotted in Fig. 12.

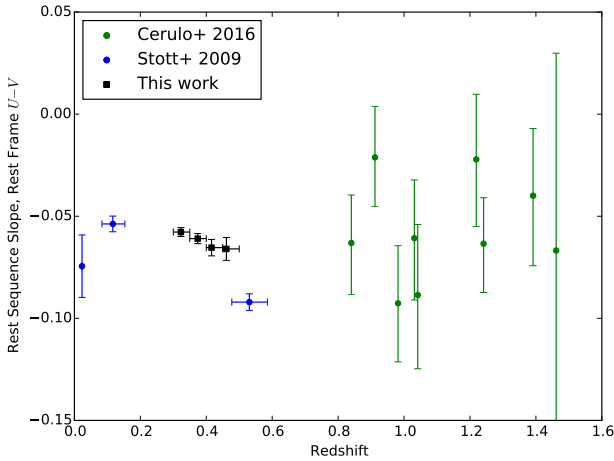


Figure 12. Our rest-frame red-sequence slope determinations compared with observations by Stott et al. (2009) and Cerulo et al. (2016). The data below $z \lesssim 0.6$ seem to show a weak decrease of slope with redshift. On the other hand, the higher-redshift data suggest no evolution since $z \sim 1.5$, subject to the admittedly large error bars. Fig. 11 specifies the binning of our data.

6.1 L_X –richness relation

Since we need *Chandra* X-ray data and *HST* SNAPshot images in both the F606W and F814W passbands to explore this relation, our sample is reduced to 22 clusters.

In recognition of the dominance of ellipticals (e.g., De Lucia & Blaizot 2007; Koester et al. 2007) within the relatively small field of view of our SNAPshot data, we use the red sequence to

Name	L_X (10^{44} erg s $^{-1}$)	X-ray peak		Rich ^c
		R.A.	Dec.	
MACSJ0011.7–1523	9.5 ± 0.1	00:11:42.88	–15:23:21.8	50
MACSJ0027.8+2616	3.8 ± 0.2	00:27:45.37	+26:16:25.7	–
MACSJ0035.4–2015	13.0 ± 0.1	00:35:26.45	–20:15:48.3	45
MACSJ0140.0–0555	8.0 ± 0.2	01:40:01.32	–05:55:07.6	50
MACSJ0150.3–1005	6.0 ± 0.1	01:50:21.30	–10:05:29.8	–
MACSJ0152.5–2852	8.2 ± 0.2	01:52:34.46	–28:53:36.3	53
MACSJ0159.8–0849	17.3 ± 0.2	01:59:49.41	–08:49:58.5	–
MACSJ0308.9+2645	15.9 ± 0.2	03:08:55.81	+26:45:37.5	58
MACSJ0404.6+1109	4.6 ± 0.2	04:04:33.34	+11:07:58.1	–
MACSJ0451.9+0006	7.3 ± 0.2	04:51:54.40	+00:06:20.3	34
MACSJ0520.7–1328	9.3 ± 0.1	05:20:42.03	–13:28:50.0	–
MACSJ0547.0–3904	6.3 ± 0.1	05:47:01.51	–39:04:26.3	27
MACSJ0712.3+5931	3.6 ± 0.1	07:12:20.75	+59:32:20.3	33
MACSJ0913.7+4056	11.3 ± 0.1	09:13:45.48	+40:56:27.5	–
MACSJ0947.2+7623	22.3 ± 0.3	09:47:13.04	+76:23:14.2	31
MACSJ0949.8+1708	11.3 ± 0.2	09:49:51.70	+17:07:08.2	36
MACSJ1006.9+3200	6.9 ± 0.2	10:06:54.57	+32:01:39.3	31
MACSJ1105.7–1014	6.9 ± 0.2	11:05:46.58	–10:14:38.9	–
MACSJ1115.2+5320	9.6 ± 0.3	11:15:15.86	+53:19:52.8	38
MACSJ1115.8+0129	16.1 ± 0.2	11:15:51.97	+01:29:55.3	–
MACSJ1142.4+5831	7.7 ± 0.1	11:42:24.01	+58:31:59.7	37
MACSJ1206.2–0847	21.1 ± 0.2	12:06:12.16	–08:48:01.4	–
MACSJ1226.8+2153C ^a	1.2 ± 0.1	12:26:41.20	+21:52:58.4	36
MACSJ1236.9+6311	6.9 ± 0.1	12:36:58.89	+63:11:12.0	36
MACSJ1319.9+7003	5.0 ± 0.1	13:20:08.44	+70:04:36.5	36
MACSJ1354.6+7715	7.0 ± 0.1	13:54:42.71	+77:15:17.1	25
MACSJ1359.1–1929	5.7 ± 0.2	13:59:10.23	–19:29:24.9	–
MACSJ1427.6–2521	5.6 ± 0.2	14:27:39.43	–25:21:02.5	–
MACSJ1452.9+5802	6.0 ± 0.1^b	14:52:57.57	+58:02:57.1	47
MACSJ1621.3+3810	8.6 ± 0.2	16:21:24.84	+38:10:08.5	32
MACSJ1731.6+2252	8.4 ± 0.2	17:31:39.07	+22:51:51.9	43
MACSJ2003.4–2322	8.7 ± 0.1	20:03:25.40	–23:24:55.5	–
MACSJ2046.0–3430	9.0 ± 0.2	20:46:00.50	–34:30:17.2	–
MACSJ2135.2–0102	6.4 ± 0.1	21:35:11.19	–01:02:55.8	29
MACSJ2211.7–0349	26.3 ± 0.3	22:11:46.00	–03:49:47.3	–
MACSJ2229.7–2755	11.0 ± 0.1	22:29:45.24	–27:55:37.2	–
MACSJ2243.3–0935	9.0 ± 0.1	22:43:21.05	–09:35:42.6	–
MACSJ2245.0+2637	9.0 ± 0.1	22:45:04.57	+26:38:04.7	–
SMACSJ0018.9–4051	3.4 ± 0.1	00:19:00.83	–40:51:55.7	–
SMACSJ0040.8–4407	7.6 ± 0.2	00:40:50.28	–44:07:52.4	–
SMACSJ0234.7–5831	8.4 ± 0.2	02:34:41.88	–58:31:25.1	34
SMACSJ0304.3–4401	7.1 ± 0.2	03:04:16.75	–44:01:32.3	–
SMACSJ0439.2–4600	4.5 ± 0.1	04:39:14.06	–46:00:50.4	–
SMACSJ0723.3–7327	15.6 ± 0.2	07:23:18.23	–73:27:16.0	36
SMACSJ2031.8–4036	8.7 ± 0.2	20:31:52.78	–40:37:24.2	24

Table 4. *Chandra* X-ray properties of our SNAP target clusters. L_X is the point-source-corrected luminosity in the 0.1–2.4 keV band.

^a This system is a triple cluster (see Mann & Ebeling 2012), of which our SNAPshots cover only one component. The X-ray peak position and X-ray luminosity apply to this component only.

^b Lower bound; target placed on chip gap.

^c Optical richness, defined as the number of galaxies within the magnitude interval $[m_3, m_3+2]$. The numbers in this column are the raw counts (of red sequence members), before application of the corrections described in the text.

determine cluster membership and define all galaxies within 3σ of the red sequence to be cluster members. This definition essentially eliminates the need to correct for interlopers from the fore- or background, in particular since projection effects are already greatly re-

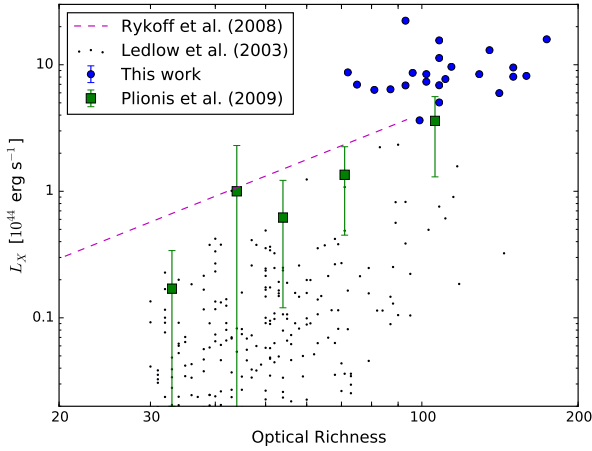


Figure 13. Correlation of X-ray luminosity (0.1–2.4 keV) with optical richness, defined as the number of red-sequence members for our work and that of Rykoff et al. (2008), and as Abell richness in the studies by Ledlow et al. (2003) and Plionis et al. (2009). Our data show a rather weak correlation ($r = 0.49$) by themselves but provide valuable leverage when combined with literature data for less massive and more nearby clusters. Note that the statistical error bars on our data are too small to be visible. Adjustments applied in order to allow a meaningful comparison between these data sets are described in the text.

duced by the relatively small angular extent⁷ of our cluster targets on the sky (Yee & López-Cruz 1999; Saro et al. 2013). Deviating slightly from the approach taken in Section 5, we limit the resulting sample of cluster members, for each cluster, by imposing a maximal magnitude differential relative to the brightness of the third-brightest galaxy (m_3). Specifically, we follow Abell (1958) and define optical richness as the number of galaxies within the magnitude interval $[m_3, m_3+2]$.

Since MACS is, by design, limited to highly X-ray luminous clusters that tend to feature a commensurately high optical richness, the range in both L_X and richness of our sample is too small to allow a determination of the L_X –richness relation from our data alone. However, our data provide a valuable complement to existing work at lower redshift for less massive clusters, such as the studies by Ledlow et al. (2003) and Plionis et al. (2009); both of these studies employ subsamples of the Abell cluster catalogue and thus use Abell’s richness counts, which employ the same magnitude interval as we do here ($[m_3, m_3+2]$). However, the $1.5\text{-}h^{-1}\text{Mpc}$ radius out to which galaxies contribute to Abell richness is far larger than the 300- to $400\text{-}h^{-1}\text{kpc}$ (radius) covered by our *HST* data. In order to account for this discrepancy, we apply a global correction factor of 3 to our richness estimates, appropriate for massive clusters at $z \sim 0.35$ (assuming the universal satellite number density profile of Budzynski et al. 2012).

We show the resulting L_X –richness relation in Fig. 13. The comparison of our results with those of Ledlow et al. (2003) and Plionis et al. (2009) illustrates another systematic effect, namely the contamination of the Abell’s richness measurements by superimposed galaxy groups or clusters (Sutherland 1988; Yee & López-Cruz 1999); such contamination artificially boosts the optical rich-

⁷ At our targets’ redshifts, our *HST* data cover only the cluster cores, i.e., a radius of 300 to $400\text{-}h^{-1}\text{kpc}$.

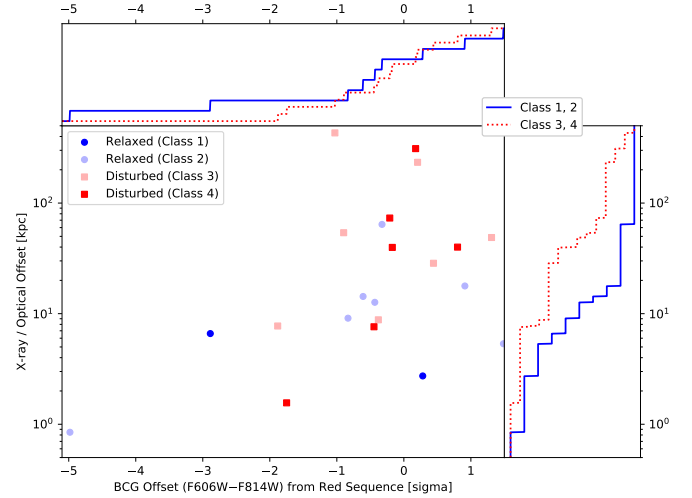


Figure 14. Offset (kpc) between the locations of the BCG and the peak of the adaptively smoothed X-ray surface brightness, as a function of the BCG’s colour offset (F606W–F814W) from the red sequence of its host cluster. The colour and shape of the various symbols indicate morphology class. The top and right-hand panels show the cumulative distribution functions for relaxed and disturbed clusters (solid and dotted lines, respectively).

ness of Abell clusters at any given X-ray luminosity. As another comparison with previous work, we also consider the L_X –richness relation determined by Rykoff et al. (2008) for the maxBCG clusters, using red-sequence galaxy counts down to $0.4L^*$ and out to a radius of $750\text{-}h^{-1}\text{kpc}$. After adjusting their results to satisfy Abell’s richness definition (in terms of depth relative to m_3 and radial extent), we find that the best-fit L_X –richness relation derived by Rykoff et al. (2008) (dashed magenta line in Fig. 13) agrees well with our data points.

We conclude that *HST* SNAPshots of MACS clusters significantly extend the dynamic range within which one can observationally establish the L_X –richness relation. A comprehensive, quantitative analysis which includes the large body of work in the existing literature will, however, require careful accounting for a number of systematic effects in the definition and determination of optical richness: these effects include the fact that observational datasets reflect different optical passbands, over a range of cluster redshifts, in various magnitude ranges, out to different radii, and with distinct approaches to fore- and background contamination corrections.

6.2 X-ray / optical offsets

For relaxed clusters, the location of the peak of the X-ray emission (Table 4) should coincide with the BCG, while for merging/disturbed clusters the different collisional properties of gas and galaxies can cause a significant X-ray/optical offset (e.g., Harvey et al. 2015; Wittman et al. 2017). However, a meaningful physical interpretation of the segregation of gas and galaxies in cluster mergers depends critically on a correct assignment of corresponding BCGs and X-ray peaks – particularly non-trivial in complex mergers that involve more than two subclusters. Given that the offsets exhibited by some of our clusters are very large (in excess of 100 kpc), we therefore caution that these large offsets may primarily reflect ambiguity regarding the choice of a single BCG for cluster mergers. Where multiple BCG candidates exist, Table 8 lists the

brightest such candidate; however, in four cases⁸ the peak X-ray emission is associated with a slightly less luminous candidate, resulting in a large X-ray/optical offset that is physically meaningful only inasmuch as it indicates the complexity of those clusters. In another case⁹ at least four plausible BCG candidates exist, and the X-ray peak does not coincide with any of them. In order to reveal the correct associations of BCGs and ICM halos, one would require a careful analysis of the distribution of dark and luminous matter in order to establish the merger history and trajectories of the individual subclusters.

We previously examined (Section 4) the connection between a BCG's colour and its internal structure; we found that the two bluest BCGs in our sample (with a red-sequence colour offset $\geq 5\sigma$) exhibit pronounced internal structure (Fig. 6) and reside in relaxed clusters (MACSJ1447.4+0827 and MACSJ0547.0–3904; see also Figs. 6 and 8). We do note that SNAPshot selection bias may affect these findings.

We now explore the relationship between a BCG's colour (its offset from its host cluster's red sequence) and its physical offset from the cluster's X-ray peak. By necessity, this investigation is limited to the clusters for which both X-ray and F606W–F814W data are available. As shown in Fig. 14, only two such clusters host BCGs significantly (more than 2.5σ) bluer than their red sequence;¹⁰ both of them exhibit relaxed morphologies characterized by small X-ray/optical offsets. These results agree with the analysis of Sanderson et al. (2009), who demonstrate that relaxed clusters are associated with stronger cool cores and greater BCG activity. In general, it appears that a relaxed morphology allows intracluster-medium cooling to focus gas accretion onto a single massive galaxy and thus revive at least some star formation. Note, however, that a relaxed host cluster and a small X-ray/optical offset are necessary but not sufficient criteria for the presence of an actively evolving BCG. As Fig. 14 demonstrates, many MACS clusters with small or moderate X-ray/optical offsets and/or relaxed morphologies do not host noticeably blue BCGs.

However, (as noted in Section 4) the F606W–F814W colour is not as sensitive to BCG star formation (at these redshifts) as the $g - r$ colour. Green et al. (2016) note the strong association between optical emission lines and significant colour offsets from the red sequence in these bands. Since their sample has ten clusters in common with ours¹¹ (Table A1 of Green et al. 2016), we use their data to plot, in Fig. 15, the X-ray/optical offset against the BCG $g - r$ offset for these clusters¹². Although this subsample is now even smaller, we find a similar trend: the two clusters with large physical offsets ($\gtrsim 20$ kpc) show only a small colour offset, whereas the clusters hosting blue BCGs are relaxed and exhibit good X-ray/optical alignment. In addition, the high resolution of our *HST* images reveals compelling evidence of star formation in these BCGs, as indicated in Fig. 8 and shown in Figs. 6 and 7.

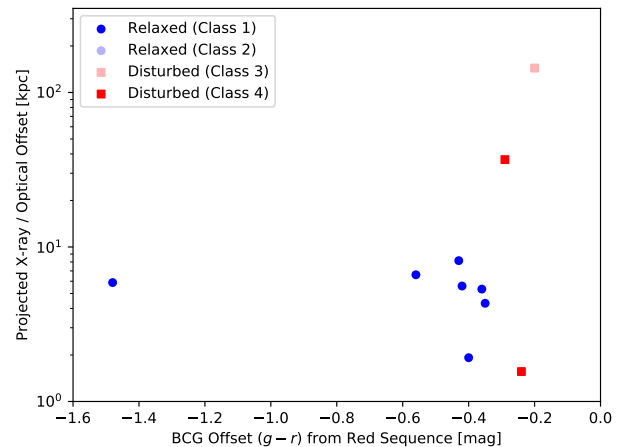


Figure 15. Offset (kpc) between BCG and X-ray peak position, as a function of the BCG's colour offset ($g - r$) from its host cluster's red sequence. The $g - r$ data come from Green et al. (2016), and in two cases (MACSJ0404.6+1109 and MACSJ2243.3–0935) we use Green et al.'s BCG identification instead of ours for the sake of consistency.

7 LEGACY VALUE

Although we hope to have demonstrated the significant discovery potential and wide applicability of the data collected in this SNAPshot survey of massive, X-ray selected clusters (see, in particular, Figs. 3, 4, 6 and 7), the true legacy value of this project is perhaps most convincingly reflected in the extensive and diverse research it has already facilitated. We therefore briefly review some of the numerous studies conducted by the extragalactic community based on these data.

Among the individual discoveries, a particularly striking object is the so-called Cosmic Eye (Smail et al. 2007) in MACSJ2135.2–0102, comprising two bright arcs generated by galaxy-galaxy lensing (panel 38 Fig. 4). The high magnification (~ 30) of the background ($z = 3.07$) Lyman-break galaxy permits detailed study of its properties, including the determination of gas fractions, stellar mass, and star-formation efficiency (Coppin et al. 2007); determination of disk rotation (Stark et al. 2008); detection of polycyclic aromatic hydrocarbon emission (Siana et al. 2009); determination of properties of its interstellar medium (Quider et al. 2010); constraints on molecular gas mass (Riechers et al. 2010); and characterization of extinction law and star formation history (Sklias et al. 2014). Dye et al. (2007), investigating the lens itself, find two spatially distinct components in the lensing galaxy, one visible, the other dark.

Focusing on other strong-lensing events discovered by MACS SNAPshot observations, Jones et al. (2010) analyse star formation and spatially resolved dynamics out to $z = 3.1$; Swinbank et al. (2011) study the kinematics of the interstellar medium in a galaxy at $z = 2.3$; and Christensen et al. (2012) perform a direct measure of oxygen abundance out to $z = 3.5$. Damjanov et al. (2013) report a population of compact galaxies at cluster redshifts (0.2–0.6), and Stark et al. (2014) rely on lensing to determine the stellar mass and star formation rate in low-luminosity/low-mass galaxies out to $z \sim 3$. More recent works include Newman et al. (2015)'s discovery of a massive, recently quenched galaxy at $z = 2.6$; Schaerer et al. (2015)'s analysis of ISM and star formation prop-

⁸ MACSJ1226.8+2153C, MACSJ2003.4–2322, SMACSJ0234.7–5831, and SMACSJ2031.8–4036

⁹ MACSJ2243.3–0935

¹⁰ Cf. Fig. 8, which displays a superset of the clusters under consideration here.

¹¹ The limited overlap is due to the fact that the groundbased imaging used by Green et al. is not deep enough to allow the red sequence to be robustly established for MACS clusters at the high end of our redshift range.

¹² In two of these cases Green et al.'s BCG identification differs from ours; for the sake of consistency, in this figure we use their BCG to mark the cluster's optical centre.

erties at $z \sim 2$; Thomson et al. (2015)’s study of cool molecular gas and star formation at $z = 2.3$, resolving scales down to 100 pc; and Patrício et al. (2016)’s radiative transfer model for a young L^* galaxy at $z \sim 3.5$. Zitrin et al. (2012) illustrates the sheer richness of the lensing accomplished by some of these clusters, finding 47 multiply-lensed images of 12 distinct sources behind MACSJ1206.2–0847. In addition, Repp et al. (2016)’s search for high-redshift galaxies behind these clusters finds ~ 20 Lyman break galaxies at $z \sim 7$ –9. Thus the lensing power of these massive clusters has been fruitful in multiple areas of research.

MACS clusters from the SNAPshot sample also serve as laboratories for the study of galaxy evolution. Again exploiting strong-lensing amplification, Livermore et al. (2012, 2015) study the evolution of star formation density and luminosity from $z = 1$ –4. Abramson et al. (2013) investigate starbursts and quenching, while multiple authors study the effects of active galactic nuclei on their host galaxies and the surrounding medium (Cavagnolo et al. 2011; Hlavacek-Larrondo et al. 2012; Ehlert et al. 2015). In addition, Zitrin (2017) reports the discovery of a rare cluster shell galaxy system in the process of formation in MACSJ1319.9+7003. Also at the cluster redshift, Ebeling et al. (2014) and McPartland et al. (2016) discover numerous dramatic examples of ram-pressure stripping in MACS SNAPshot data (‘jellyfish galaxies’) – a most spectacular (and violent) phase of galaxy evolution.

Studies of the MACS SNAPshot clusters as a whole have also been fruitful. Ebeling et al. (2009) conclude that the cluster MACSJ1206.2–0847 is undergoing a line-of-sight merger event, and Ho et al. (2012) analyse the merger history of MACS J0140.0–0555. Both Stott et al. (2007) and De Propriis et al. (2013) study the evolution of the cluster member population, and Horesh et al. (2010) compare the arc-production efficiencies of X-ray selected and optically selected clusters. The colour information and high resolution afforded by the *HST* images also allow construction of dark matter mass profiles for these clusters (Richard et al. 2015; Zitrin & Broadhurst 2016; see also Richard et al. in prep.).

The SNAPshot images also permit study of more general cosmological questions. Gilmore & Natarajan (2009) investigate the feasibility of constraining the dark energy equation of state by stacking images from strongly lensed clusters, while Harvey et al. (2015) constrain the self-interaction cross-section of dark matter by considering cluster mergers.

Last, but certainly not least, our *HST* SNAPshot surveys of MACS clusters serve as pathfinder missions for more focused efforts. Just as MACS first discovered three out of the six Hubble Frontier Fields¹³ targets (another two are MACS re-discoveries), this particular SNAPshot survey has provided a significant number of targets for the *HST* legacy programme CLASH (Cluster Lensing And Supernova survey with Hubble – Postman et al. 2012) and has also contributed heavily to the more recent RELICS¹⁴ (REionization LensIng Cluster Survey) project.

Finally, we point out that, by virtue of the information listed in Table 8, this paper also constitutes the largest release of MACS cluster redshifts to the community to date, complementing the partial releases published by Ebeling et al. (2007, 2010) and Mann & Ebeling (2012).

8 CONCLUSION

The value of SNAPshot surveys rests largely on the richness and diversity of data obtained with a relatively small investment of *HST* observing time. This paper provides examples illustrating the wide range of astrophysical topics investigable with this data set, either alone or in combination with other observations. As a broad overview of selected topics (rather than an exhaustive catalog of all of them, or an in-depth study of any), our treatment is cursory by necessity. Section 7 has reviewed other, more in-depth treatments of various areas of research using these data.

Nevertheless, even our cursory analysis demonstrates the power of SNAPshot observations specifically for investigations relying on strong gravitational lensing, where the plethora of spectacular arcs and multiple-image systems discovered by our project (Figs. 3, 4) advances three distinct fields at once by (a) allowing the mapping of all gravitational matter, dark or luminous, in massive clusters; (b) identifying the best targets for in-depth study of highly magnified background galaxies; and (c) helping to constrain the properties of the first populations of galaxies at $z > 6$. Similarly, the high-resolution images of BCGs in massive clusters at $z > 0.3$ obtained by our SNAPshots (Figs. 6, 7) ideally complement existing and ongoing studies aimed at identifying the interplay of accretion, star formation, AGN feedback, and mergers in the formation and growth of these extreme stellar systems. Although far from exhaustive, the work presented here has also revealed three distinct lines of evidence (rest-frame slope of the red sequence, BCG colours, distribution and relative frequency of cluster morphology classes) supporting the notion that the general features of massive cluster morphology were in place well before $z = 0.5$, i.e., well over 5 Gyr ago, with no strong evolution in the $z = 0.3$ –0.5 range. Ongoing *HST* SNAPshot observations of eMACS clusters at $z > 0.5$ (Ebeling et al. 2013) – which probe the population of extremely X-ray luminous clusters out to $z \sim 1$ – stand to shed light on the yet earlier history of these exceptional objects. Finally, by probing the previously poorly sampled regime of very massive clusters at intermediate redshift, the MACS SNAPshot survey also adds crucial leverage to scaling relations such as that between X-ray luminosity and optical richness (Fig. 13).

Most importantly, however, our *HST* SNAPshot surveys of MACS clusters have established their value as pathfinder missions for the entire extragalactic community. This programme has created a legacy dataset of high-resolution images of some of the most extreme galaxy clusters known. It thus has enabled countless discoveries, and it will continue to facilitate further in-depth study of galaxy evolution and structure formation, from the cluster redshifts to lensing-assisted probes of the elusive era of re-ionization.

ACKNOWLEDGEMENTS

We thank Alastair Edge for inspiring conversations and helpful comments on all matters BCG; we also appreciate insightful suggestions from both Ian Smail and an anonymous referee. The authors gratefully acknowledge financial support from STScI grants GO-10491, GO-10875, GO-12166, and GO-12884.

The scientific results reported in this article are based on observations made with the NASA/ESA Hubble Space Telescope, obtained at the Space Telescope Science Institute, which is operated by the Association of Universities for Research in Astronomy, Inc., under NASA contract NAS 5-26555. The results are also based in part on observations made by the Chandra X-ray Observatory.

¹³ <http://www.stsci.edu/hst/campaigns/frontier-fields/>

¹⁴ <https://relics.stsci.edu/>

In addition, some of the data presented herein were obtained at the W.M. Keck Observatory, which is operated as a scientific partnership among the California Institute of Technology, the University of California, and the National Aeronautics and Space Administration. The Observatory was made possible by the generous financial support of the W.M. Keck Foundation.

Finally, the authors wish to recognize and acknowledge the very significant cultural role and reverence that the summit of Mauna Kea has always had within the indigenous Hawaiian community. We are most fortunate to have the opportunity to conduct observations from this mountain.

REFERENCES

- Abell G. O., 1958, *ApJS*, **3**, 211
- Abramson L. E., Dressler A., Gladders M. D., Oemler Jr. A., Poggianti B. M., Monson A., Persson E., et al., 2013, *ApJ*, **777**, 124
- Andreon S., Newman A. B., Trinchieri G., Raichoor A., Ellis R. S., Treu T., 2014, *A&A*, **565**, A120
- Avila R. J., 2017, Advanced Camera for Surveys Instrument Handbook for Cycle 25 v. 16.0
- Bartelmann M., Huss A., Colberg J. M., Jenkins A., Pearce F. R., 1998, *A&A*, **330**, 1
- Begelman M. C., Blandford R. D., Rees M. J., 1980, *Nature*, **287**, 307
- Bertin E., Arnouts S., 1996, *A&AS*, **117**, 393
- Bildfell C., Hoekstra H., Babul A., Mahdavi A., 2008, *MNRAS*, **389**, 1637
- Bleem L. E., Stalder B., de Haan T., Aird K. A., Allen S. W., Applegate D. E., Ashby M. L. N., et al., 2015, *ApJS*, **216**, 27
- Böhringer H., et al., 2004, *A&A*, **425**, 367
- Boller T., Freyberg M. J., Trümper J., Haberl F., Voges W., Nandra K., 2016, *A&A*, **588**, A103
- Bower R. G., Lucey J. R., Ellis R. S., 1992, *MNRAS*, **254**, 601
- Bradač M., Allen S. W., Treu T., Ebeling H., Massey R., Morris R. G., von der Linden A., Applegate D., 2008, *ApJ*, **687**, 959
- Bruzual G., Charlot S., 2003, *MNRAS*, **344**, 1000
- Budzynski J. M., Koposov S. E., McCarthy I. G., McGee S. L., Belokurov V., 2012, *MNRAS*, **423**, 104
- Cavagnolo K. W., McNamara B. R., Wise M. W., Nulsen P. E. J., Brüggemann M., Gitti M., Rafferty D. A., 2011, *ApJ*, **732**, 71
- Cerulo P., et al., 2016, *MNRAS*, **457**, 2209
- Christensen L., Laursen P., Richard J., Hjorth J., Milvang-Jensen B., Dessauges-Zavadsky M., Limousin M., et al., 2012, *MNRAS*, **427**, 1973
- Coppin K. E. K., Swinbank A. M., Neri R., Cox P., Smail I., Ellis R. S., Geach J. E., et al., 2007, *ApJ*, **665**, 936
- Dalal N., Holder G., Hennawi J. F., 2004, *ApJ*, **609**, 50
- Damjanov I., Chilingarian I., Hwang H. S., Geller M. J., 2013, *ApJ*, **775**, L48
- De Lucia G., Blaizot J., 2007, *MNRAS*, **375**, 2
- De Lucia G., et al., 2007, *MNRAS*, **374**, 809
- De Propriis R., Philipps S., Bremer M. N., 2013, *MNRAS*, **434**, 3469
- Dressler L., 2017, Wide Field Camera 3 Instrument Handbook, Version 9.0
- Dye S., Smail I., Swinbank A. M., Ebeling H., Edge A. C., 2007, *MNRAS*, **379**, 308
- Ebeling H., Edge A. C., Bohringer H., Allen S. W., Crawford C. S., Fabian A. C., Voges W., Huchra J. P., 1998, *MNRAS*, **301**, 881
- Ebeling H., Edge A. C., Allen S. W., Crawford C. S., Fabian A. C., Huchra J. P., 2000, *MNRAS*, **318**, 333
- Ebeling H., Edge A. C., Henry J. P., 2001, *ApJ*, **553**, 668
- Ebeling H., White D. A., Rangarajan F. V. N., 2006, *MNRAS*, **368**, 65
- Ebeling H., Barrett E., Donovan D., Ma C.-J., Edge A. C., van Speybroeck L., 2007, *ApJ*, **661**, L33
- Ebeling H., Ma C. J., Kneib J.-P., Jullo E., Courtney N. J. D., Barrett E., Edge A. C., et al., 2009, *MNRAS*, **395**, 1213
- Ebeling H., Edge A. C., Mantz A., Barrett E., Henry J. P., Ma C. J., van Speybroeck L., 2010, *MNRAS*, **407**, 83
- Ebeling H., Edge A. C., Burgett W. S., Chambers K. C., Hodapp K. W., Huber M. E., Kaiser N., et al., 2013, *MNRAS*, **432**, 62
- Ebeling H., Stephenson L. N., Edge A. C., 2014, *ApJ*, **781**, L40
- Edge A. C., 2001, *MNRAS*, **328**, 762
- Edwards L. O. V., Hudson M. J., Balogh M. L., Smith R. J., 2007, *MNRAS*, **379**, 100
- Ehlert S., Allen S. W., Brandt W. N., Canning R. E. A., Luo B., Mantz A., Morris R. G., et al., 2015, *MNRAS*, **446**, 2709
- Gilmore J., Natarajan P., 2009, *MNRAS*, **396**, 354
- Gladders M. D., López-Cruz O., Yee H. K. C., Kodama T., 1998, *ApJ*, **501**, 571
- Gladders M. D., Hoekstra H., Yee H. K. C., Hall P. B., Barrientos L. F., 2003, *ApJ*, **593**, 48
- Green T. S., Edge A. C., Stott J. P., Ebeling H., Burgett W. S., Chambers K. C., Draper P. W., et al., 2016, *MNRAS*, **461**, 560
- Harvey D., Massey R., Kitching T., Taylor A., Tittley E., 2015, *Science*, **347**, 1462
- Hlavacek-Larrondo J., Fabian A. C., Edge A. C., Ebeling H., Sanders J. S., Hogan M. T., Taylor G. B., 2012, *MNRAS*, **421**, 1360
- Ho I.-T., Ebeling H., Richard J., 2012, *MNRAS*, **426**, 1992
- Horesh A., Ofek E. O., Maoz D., Bartelmann M., Meneghetti M., Rix H.-W., 2005, *ApJ*, **633**, 768
- Horesh A., Maoz D., Ebeling H., Seidel G., Bartelmann M., 2010, *MNRAS*, **406**, 1318
- Horesh A., Maoz D., Hilbert S., Bartelmann M., 2011, *MNRAS*, **418**, 54
- Hudson M. J., Ebeling H., 1997, *ApJ*, **479**, 621
- Jaffé Y. L., Aragón-Salamanca A., De Lucia G., Jablonka P., Rudnick G., Saglia R., Zaritsky D., 2011, *MNRAS*, **410**, 280
- Johnstone R. M., Fabian A. C., Nulsen P. E. J., 1987, *MNRAS*, **224**, 75
- Jones T. A., Swinbank A. M., Ellis R. S., Richard J., Stark D. P., 2010, *MNRAS*, **404**, 1247
- Kashlinsky A., Atrio-Barandela F., Ebeling H., Edge A., Kocevski D., 2010, *ApJ*, **712**, L81
- Kneib J.-P., Natarajan P., 2011, *A&A Rev.*, **19**, 47
- Kocevski D. D., Ebeling H., Mullis C. R., Tully R. B., 2007, *ApJ*, **662**, 224
- Kodama T., Arimoto N., 1997, *A&A*, **320**, 41
- Koester B. P., et al., 2007, *ApJ*, **660**, 239
- Laine S., van der Marel R. P., Lauer T. R., Postman M., O’Dea C. P., Owen F. N., 2003, *AJ*, **125**, 478
- Lauer T. R., Postman M., 1994, *ApJ*, **425**, 418
- Ledlow M. J., Voges W., Owen F. N., Burns J. O., 2003, *AJ*, **126**, 2740
- Livermore R. C., Jones T., Richard J., Bower R. G., Ellis R. S., Swinbank A. M., Rigby J. R., et al., 2012, *MNRAS*, **427**, 688
- Livermore R. C., Jones T. A., Richard J., Bower R. G., Swinbank A. M., Yuan T.-T., Edge A. C., et al., 2015, *MNRAS*, **450**, 1812
- López-Cruz O., 1997, PhD thesis, University of Toronto (LC97), (1997)
- López-Cruz O., Barkhouse W. A., Yee H. K. C., 2004, *ApJ*, **614**, 679
- Mann A. W., Ebeling H., 2012, *MNRAS*, **420**, 2120
- Mantz A., Allen S. W., Ebeling H., Rapetti D., 2008, *MNRAS*, **387**, 1179
- Mantz A., Allen S. W., Rapetti D., Ebeling H., 2010a, *MNRAS*, **406**, 1759
- Mantz A., Allen S. W., Ebeling H., Rapetti D., Drlica-Wagner A., 2010b, *MNRAS*, **406**, 1773
- Mantz A. B., Allen S. W., Morris R. G., Rapetti D. A., Applegate D. E., Kelly P. L., von der Linden A., Schmidt R. W., 2014, *MNRAS*, **440**, 2077
- Markevitch M., Gonzalez A. H., Clowe D., Vikhlinin A., Forman W., Jones C., Murray S., Tucker W., 2004, *ApJ*, **606**, 819
- Marriage T. A., Acquaviva V., Ade P. A. R., Aguirre P., Amiri M., Appel J. W., Barrientos L. F., et al., 2011, *ApJ*, **737**, 61
- McPartland C., Ebeling H., Roediger E., Blumenthal K., 2016, *MNRAS*, **455**, 2994
- Mei S., Holden B. P., Blakeslee J. P., Ford H. C., Franx M., Homeier N. L., Illingworth G. D., et al., 2009, *ApJ*, **690**, 42
- Meneghetti M., Bartelmann M., Moscardini L., 2003, *MNRAS*, **340**, 105
- Meneghetti M., Fedeli C., Pace F., Gottlöber S., Yepes G., 2010, *A&A*, **519**, A90
- Meneghetti M., Fedeli C., Zitrin A., Bartelmann M., Broadhurst T., Gottlöber S., Moscardini L., Yepes G., 2011, *A&A*, **530**, A17

- Meneghetti M., Bartelmann M., Dahle H., Limousin M., 2013, *Space Sci. Rev.*, **177**, 31
- Merten J., Coe D., Dupke R., Massey R., Zitrin A., Cypriano E. S., Okabe N., et al., 2011, *MNRAS*, **417**, 333
- Newman A. B., Belli S., Ellis R. S., 2015, *ApJ*, **813**, L7
- Oguri M., Lee J., Suto Y., 2003, *ApJ*, **599**, 7
- Oke J. B., Gunn J. E., 1983, *ApJ*, **266**, 713
- Patrício V., Richard J., Verhamme A., Wisotzki L., Brinchmann J., Turner M. L., Christensen L., et al., 2016, *MNRAS*, **456**, 4191
- Pimblet K. A., Smail I., Edge A. C., Couch W. J., O'Hely E., Zabludoff A. I., 2001, *MNRAS*, **327**, 588
- Pimblet K. A., Smail I., Edge A. C., O'Hely E., Couch W. J., Zabludoff A. I., 2006, *MNRAS*, **366**, 645
- Planck Collaboration Ade P. A. R., Aghanim N., Armitage-Caplan C., Arnaud M., Ashdown M., Atrio-Barandela F., et al., 2014, *A&A*, **571**, A20
- Planck Collaboration Ade P. A. R., Aghanim N., Arnaud M., Ashdown M., Aumont J., Baccigalupi C., et al., 2015, *A&A*, **582**, A29
- Planck Collaboration Ade P. A. R., Aghanim N., Argüeso F., Arnaud M., Ashdown M., Aumont J., et al., 2016, *A&A*, **594**, A26
- Plionis M., Tovmassian H. M., Andernach H., 2009, *MNRAS*, **395**, 2
- Postman M., Coe D., Benítez N., Bradley L., Broadhurst T., Donahue M., Ford H., et al., 2012, *ApJS*, **199**, 25
- Quider A. M., Shapley A. E., Pettini M., Steidel C. C., Stark D. P., 2010, *MNRAS*, **402**, 1467
- Quillen A. C., Zufelt N., Park J., O'Dea C. P., Baum S. A., Privon G., Noel-Storr J., et al., 2008, *ApJS*, **176**, 39
- Reichert A., Böhringer H., Fassbender R., Mühlegger M., 2011, *A&A*, **535**, A4
- Repp A., Ebeling H., Richard J., 2016, *MNRAS*, **457**, 1399
- Richard J., Patricio V., Martinez J., Bacon R., Clément B., Weilbacher P., Soto K., et al., 2015, *MNRAS*, **446**, L16
- Riechers D. A., Carilli C. L., Walter F., Momjian E., 2010, *ApJ*, **724**, L153
- Rykoff E. S., McKay T. A., Becker M. R., Evrard A., Johnston D. E., Koester B. P., Rozo E., et al., 2008, *ApJ*, **675**, 1106
- Sanderson A. J. R., Edge A. C., Smith G. P., 2009, *MNRAS*, **398**, 1698
- Saro A., Mohr J. J., Bazin G., Dolag K., 2013, *ApJ*, **772**, 47
- Schaerer D., Boone F., Jones T., Dessauges-Zavadsky M., Sklias P., Zamojski M., Cava A., et al., 2015, *A&A*, **576**, L2
- Schindler S., Castillo-Morales A., De Filippis E., Schwöpe A., Wambsgans J., 2001, *A&A*, **376**, L27
- Siana B., et al., 2009, *ApJ*, **698**, 1273
- Sklias P., Zamojski M., Schaefer D., Dessauges-Zavadsky M., Egami E., Rex M., Rawle T., et al., 2014, *A&A*, **561**, A149
- Smail I., Swinbank A. M., Richard J., Ebeling H., Kneib J.-P., Edge A. C., Stark D., et al., 2007, *ApJ*, **654**, L33
- Smith R. J., et al., 2008, *MNRAS*, **386**, L96
- Song J., Mohr J. J., Barkhouse W. A., Warren M. S., Dolag K., Rude C., 2012, *ApJ*, **747**, 58
- Spitler L. R., Labbé I., Glazebrook K., Persson S. E., Monson A., Papovich C., Tran K.-V. H., et al., 2012, *ApJ*, **748**, L21
- Stanek R., Evrard A. E., Böhringer H., Schuecker P., Nord B., 2006, *ApJ*, **648**, 956
- Stark D. P., Swinbank A. M., Ellis R. S., Dye S., Smail I. R., Richard J., 2008, *Nature*, **455**, 775
- Stark D. P., Richard J., Siana B., Charlot S., Freeman W. R., Gutkin J., Wofford A., et al., 2014, *MNRAS*, **445**, 3200
- Stott J. P., Smail I., Edge A. C., Ebeling H., Smith G. P., Kneib J.-P., Pimblet K. A., 2007, *ApJ*, **661**, 95
- Stott J. P., Pimblet K. A., Edge A. C., Smith G. P., Wardlow J. L., 2009, *MNRAS*, **394**, 2098
- Stott J. P., Hickox R. C., Edge A. C., Collins C. A., Hilton M., Harrison C. D., Romer A. K., et al., 2012, *MNRAS*, **422**, 2213
- Sunyaev R. A., Zeldovich Y. B., 1972, *Comments on Astrophysics and Space Physics*, **4**, 173
- Sutherland W., 1988, *MNRAS*, **234**, 159
- Swinbank A. M., Papadopoulos P. P., Cox P., Krips M., Ivison R. J., Smail I., Thomson A. P., et al., 2011, *ApJ*, **742**, 11
- Tanaka M., De Breuck C., Venemans B., Kurk J., 2010, *A&A*, **518**, A18
- Thomas J., Saglia R. P., Bender R., Erwin P., Fabricius M., 2014, *ApJ*, **782**, 39
- Thomson A. P., Ivison R. J., Owen F. N., Danielson A. L. R., Swinbank A. M., Smail I., 2015, *MNRAS*, **448**, 1874
- Torri E., Meneghetti M., Bartelmann M., Moscardini L., Rasia E., Tormen G., 2004, *MNRAS*, **349**, 476
- Voges W., Aschenbach B., Böller T., Bräuninger H., Briel U., Burkert W., Dennerl K., et al., 1999, *A&A*, **349**, 389
- Wen Z. L., Han J. L., 2013, *MNRAS*, **436**, 275
- Werner N., Oonk J. B. R., Sun M., Nulsen P. E. J., Allen S. W., Canning R. E. A., Simionescu A., et al., 2014, *MNRAS*, **439**, 2291
- Williamson R., Benson B. A., High F. W., Vanderlinde K., Ade P. A. R., Aird K. A., Andersson K., et al., 2011, *ApJ*, **738**, 139
- Wittman D., Golovich N., Dawson W. A., 2017, preprint, ([arXiv:1701.05877](https://arxiv.org/abs/1701.05877))
- Xu B., Postman M., Meneghetti M., Seitz S., Zitrin A., Merten J., Maoz D., et al., 2016, *ApJ*, **817**, 85
- Yee H. K. C., López-Cruz O., 1999, *AJ*, **117**, 1985
- Zaritsky D., Gonzalez A. H., 2003, *ApJ*, **584**, 691
- Zhang Y.-Y., Reiprich T. H., Schneider P., Clerc N., Merloni A., Schwöpe A., Borm K., et al., 2017, *A&A*, **599**, A138
- Zitrin A., 2017, *ApJ*, **834**, 45
- Zitrin A., Broadhurst T., 2016, *ApJ*, **833**, 25
- Zitrin A., Rosati P., Nonino M., Grillo C., Postman M., Coe D., Seitz S., et al., 2012, *ApJ*, **749**, 97
- von der Linden A., Allen M. T., Applegate D. E., Kelly P. L., Allen S. W., Ebeling H., Burchat P. R., et al., 2014, *MNRAS*, **439**, 2

Name	Right Ascension	Declination	F606	F814	F110W	F140W	z	z reference	Morphology X-ray Optical
MACSJ0011.7–1523	00:11:42.8	–15:23:22	Y	Y	–	–	0.379	(2)	1 2
MACSJ0027.8+2616	00:27:45.8	+26:16:26	Y	–	Y	Y	0.360	(1)	2 2
MACSJ0032.1+1808	00:32:10.6	+18:07:39	Y	Y	–	–	0.377	(1)	– 4
MACSJ0033.8–0751	00:33:52.2	–07:51:12	–	Y	–	–	0.305	(1)	– 4
MACSJ0034.4+0225	00:34:26.1	+02:25:33	–	Y	–	–	0.388	(1)	– 3
MACSJ0034.9+0234	00:34:57.8	+02:33:32	–	Y	–	–	0.390	(1)	– 2
MACSJ0035.4–2015	00:35:26.1	–20:15:45	Y	Y	–	–	0.353	(2)	3 2
MACSJ0051.6+2720	00:51:38.6	+27:19:60	–	–	Y	Y	0.364	(1)	– 2
MACSJ0110.1+3211	01:10:07.2	+32:10:48	Y	Y	–	–	0.341	(1)	– 2
MACSJ0140.0–0555	01:40:00.0	–05:54:57	Y	Y	Y	Y	0.451	(3)	3 3
MACSJ0140.0–3410	01:40:05.5	–34:10:38	Y	–	–	–	0.395	(1)	– 1
MACSJ0150.3–1005	01:50:21.2	–10:05:31	–	Y	Y	Y	0.363	(1)	1 1
MACSJ0152.5–2852	01:52:34.5	–28:53:37	Y	Y	Y	Y	0.412	(2)	2 3
MACSJ0159.8–0849	01:59:49.3	–08:49:59	Y	–	–	–	0.407	(2)	1 1
MACSJ0242.5–2132	02:42:35.9	–21:32:26	Y	–	–	–	0.314	(2)	1 1
MACSJ0257.6–2209	02:57:41.1	–22:09:18	Y	Y	Y	Y	0.322	(2)	– 2
MACSJ0308.9+2645	03:08:57.6	+26:45:33	Y	Y	–	–	0.356	(2)	3 2
MACSJ0404.6+1109	04:04:33.1	+11:08:07	–	Y	–	–	0.358	(2)	4 3
MACSJ0449.3–2848	04:49:20.7	–28:49:09	Y	–	–	–	0.327	(1)	– 2
MACSJ0451.9+0006	04:51:54.6	+00:06:18	Y	Y	Y	Y	0.429	(3)	2 3
MACSJ0520.7–1328	05:20:42.0	–13:28:47	Y	–	Y	Y	0.336	(2)	2 3
MACSJ0521.4–2754	05:21:26.2	–27:54:42	Y	Y	–	–	0.314	(1)	– 3
MACSJ0547.0–3904	05:47:01.5	–39:04:26	Y	Y	–	–	0.319	(2)	2 3
MACSJ0600.1–2008	06:00:08.6	–20:07:36	–	Y	–	–	0.427	(1)	– 4
MACSJ0611.8–3036	06:11:49.6	–30:38:09	–	–	Y	Y	0.320	(1)	– 4
MACSJ0712.3+5931	07:12:20.5	+59:32:20	Y	Y	Y	Y	0.328	(1)	2 1
MACSJ0845.4+0327	08:45:27.8	+03:27:39	Y	Y	–	–	0.329	(1)	– 2
MACSJ0913.7+4056	09:13:45.5	+40:56:28	Y	–	–	–	0.442	(3)	1 1
MACSJ0916.1–0023	09:16:11.6	–00:23:36	Y	Y	Y	Y	0.320	(1)	– 4
MACSJ0947.2+7623	09:47:12.8	+76:23:14	Y	Y	Y	Y	0.354	(2)	1 1
MACSJ0949.8+1708	09:49:51.8	+17:07:10	Y	Y	–	–	0.384	(2)	2 3
MACSJ1006.9+3200	10:06:55.4	+32:00:54	Y	Y	–	–	0.403	(3)	4 4
MACSJ1105.7–1014	11:05:46.8	–10:14:46	Y	–	–	–	0.415	(3)	2 2
MACSJ1115.2+5320	11:15:16.2	+53:19:36	Y	Y	Y	Y	0.466	(3)	3 3
MACSJ1115.8+0129	11:15:51.9	+01:29:55	Y	–	–	–	0.354	(2)	1 1
MACSJ1124.5+4351	11:24:29.8	+43:51:26	Y	Y	Y	Y	0.368	(1)	– 1
MACSJ1133.2+5008	11:33:13.0	+50:08:25	Y	Y	Y	Y	0.389	(1)	– 3
MACSJ1141.6–1905	11:41:41.0	–19:05:21	–	–	Y	Y	0.305	(1)	– 3
MACSJ1142.4+5831	11:42:24.3	+58:31:47	Y	Y	Y	Y	0.326	(1)	4 4
MACSJ1206.2–0847	12:06:12.1	–08:48:03	Y	–	–	–	0.439	(2)	2 2
MACSJ1226.8+2153C ^a	12:26:42.5	+21:52:55	Y	Y	Y	Y	0.437	(3)	– 3
MACSJ1236.9+6311	12:37:00.6	+63:11:12	Y	Y	Y	Y	0.302	(1)	3 2
MACSJ1258.0+4702	12:58:03.3	+47:02:58	Y	Y	–	–	0.331	(1)	– 2
MACSJ1319.9+7003	13:20:08.4	+70:04:39	Y	Y	Y	Y	0.327	(2)	2 1
MACSJ1328.2+5244	13:28:13.6	+52:43:47	Y	Y	–	–	0.321	(1)	– 3
MACSJ1354.6+7715	13:54:25.3	+77:15:35	Y	Y	Y	Y	0.397	(1)	4 4
MACSJ1359.1–1929	13:59:10.2	–19:29:25	–	Y	Y	Y	0.447	(3)	1 1
MACSJ1427.6–2521	14:27:39.5	–25:21:02	–	Y	–	–	0.318	(2)	1 1
MACSJ1447.4+0827	14:47:26.0	+08:28:25	Y	Y	–	–	0.376	(3)	– 1
MACSJ1452.9+5802	14:52:55.5	+58:02:39	Y	Y	–	–	0.324	(1)	– 4
MACSJ1526.7+1647	15:26:42.5	+16:47:32	Y	–	Y	Y	0.338	(1)	– 3
MACSJ1551.9–0207	15:51:58.5	–02:07:50	–	Y	Y	Y	0.300	(1)	– 1
MACSJ1621.3+3810	16:21:24.8	+38:10:09	Y	Y	Y	Y	0.465	(3)	1 2
MACSJ1625.7–0830	16:25:45.9	–08:30:55	–	Y	Y	Y	0.464	(1)	– 2
MACSJ1644.9+0139	16:45:00.8	+01:40:01	Y	Y	–	–	0.336	(1)	– 3
MACSJ1652.3+5534	16:52:18.7	+55:34:58	Y	Y	Y	Y	0.324	(1)	– 1
MACSJ1731.6+2252	17:31:39.0	+22:52:11	Y	Y	Y	Y	0.389	(2)	4 4
MACSJ1738.1+6006	17:38:06.9	+60:06:18	Y	Y	Y	Y	0.329	(1)	– 1

Table 5. MACS clusters with *Hubble* SNAPshots. For explanation of morphology codes see Section 2. Redshift references: (1) this work; (2) Ebeling et al. (2010); (3) Mann & Ebeling (2012).

^a See (3) for overall morphology of this three-component cluster configuration.

Name	Right Ascension	Declination	F606	F814	F110W	F140W	z	z reference	Morphology X-ray Optical
MACSJ1752.0+4440	17:51:58.8	+44:39:36	Y	Y	Y	Y	0.364	(1)	– 4
MACSJ1806.8+2931	18:06:52.4	+29:30:13	Y	Y	–	–	0.300	(1)	– 1
MACSJ2003.4–2322	20:03:29.7	–23:24:25	–	Y	Y	Y	0.316	(1)	4 4
MACSJ2046.0–3430	20:46:00.5	–34:30:18	–	–	Y	Y	0.423	(3)	1 2
MACSJ2050.7+0123	20:50:42.4	+01:23:39	Y	Y	Y	Y	0.333	(1)	– 3
MACSJ2051.1+0215	20:51:10.9	+02:16:05	Y	Y	Y	Y	0.321	(1)	– 3
MACSJ2134.6–2706	21:34:36.0	–27:05:56	–	Y	–	–	0.363	(1)	– 2
MACSJ2135.2–0102	21:35:12.1	–01:02:59	Y	Y	Y	Y	0.325	(1)	2 3
MACSJ2149.3+0951	21:49:19.7	+09:51:37	Y	Y	–	–	0.375	(1)	– 2
MACSJ2211.7–0349	22:11:45.9	–03:49:45	Y	–	–	–	0.397	(2)	2 2
MACSJ2229.7–2755	22:29:45.2	–27:55:36	–	–	Y	Y	0.324	(2)	1 1
MACSJ2241.8+1732	22:41:56.6	+17:32:43	Y	Y	–	–	0.317	(1)	– 4
MACSJ2243.3–0935	22:43:20.4	–09:35:22	Y	–	–	–	0.447	(2)	3 4
MACSJ2245.0+2637	22:45:04.7	+26:38:05	–	–	Y	Y	0.301	(2)	1 2
MACSJ2245.4+2808	22:45:24.1	+28:08:01	–	Y	–	–	0.340	(1)	– 4
SMACSJ0018.9–4051	00:19:01.5	–40:51:50	Y	–	–	–	0.477	(1)	2 –
SMACSJ0040.8–4407	00:40:50.1	–44:07:49	–	–	Y	Y	0.363	(1)	2 –
SMACSJ0234.7–5831	02:34:46.1	–58:31:07	Y	Y	Y	Y	0.408	(1)	1 3
SMACSJ0304.3–4401	03:04:16.9	–44:01:31	Y	–	–	–	0.460	(1)	4 –
SMACSJ0332.8–8452	03:33:06.6	–84:53:42	–	–	Y	Y	0.370	(1)	– –
SMACSJ0439.2–4600	04:39:14.0	–46:00:49	Y	–	–	–	0.320	(1)	1 –
SMACSJ0549.3–6205	05:49:17.0	–62:05:11	Y	Y	Y	Y	0.375	(1)	– 4
SMACSJ0600.2–4353	06:00:17.5	–43:53:19	Y	Y	Y	Y	0.300	(1)	– 4
SMACSJ0723.3–7327	07:23:22.7	–73:27:14	Y	Y	–	–	0.404	(1)	3 4
SMACSJ1519.1–8130	15:18:48.7	–81:30:14	Y	–	–	–	0.480	(1)	– –
SMACSJ2031.8–4036	20:31:50.7	–40:37:15	Y	Y	Y	Y	0.342	(1)	3 4
SMACSJ2131.1–4019	21:31:05.0	–40:19:21	Y	Y	Y	Y	0.421	(1)	– 1
SMACSJ2332.4–5358	23:32:27.5	–53:58:29	–	–	Y	Y	0.403	(1)	– –

Table 5 – *continued* MACS clusters with *Hubble* SNAPshots. For explanation of morphology codes see Section 2. Redshift references: (1) this work; (2) Ebeling et al. (2010); (3) Mann & Ebeling (2012).

ClusterBCG.....		G2.....			band
	mag ^a	RA	Dec	mag ^a	RA	Dec	
MACSJ0011.7–1523	18.40	00:11:42.84	–15:23:21.7	18.98	00:11:45.69	–15:24:50.6	F814W
MACSJ0027.8+2616	19.20	00:27:45.79	+26:16:26.5	19.45	00:27:43.69	+26:16:21.4	F606W
MACSJ0032.1+1808	18.50	00:32:09.41	+18:06:55.7	18.72	00:32:08.23	+18:06:25.0	F814W
MACSJ0033.8–0751	17.57	00:33:51.30	–07:50:15.5	17.89	00:33:53.14	–07:52:10.5	F814W
MACSJ0034.4+0225	18.52	00:34:28.16	+02:25:22.3	18.53	00:34:25.98	+02:25:24.9	F814W
MACSJ0034.9+0234	17.71	00:34:57.82	+02:33:31.5	18.28	00:34:56.79	+02:33:18.7	F814W
MACSJ0035.4–2015	17.82	00:35:26.12	–20:15:44.9	19.28	00:35:22.99	–20:14:35.7	F814W
MACSJ0051.6+2720	16.32	00:51:38.59	+27:19:59.9	18.04	00:51:41.62	+27:20:01.5	F110W
MACSJ0110.1+3211	18.04	01:10:07.19	+32:10:48.5	18.85	01:10:06.97	+32:10:28.4	F814W
MACSJ0140.0–0555	18.44	01:40:00.83	–05:55:03.2	19.01	01:40:03.20	–05:55:21.8	F814W
MACSJ0140.0–3410	19.53	01:40:05.48	–34:10:38.3	20.10	01:40:01.24	–34:09:48.2	F606W
MACSJ0150.3–1005	17.29	01:50:21.25	–10:05:30.7	19.15	01:50:18.40	–10:05:12.0	F814W
MACSJ0152.5–2852	18.93	01:52:34.49	–28:53:37.2	19.01	01:52:33.73	–28:55:18.4	F814W
MACSJ0159.8–0849	18.89	01:59:49.31	–08:49:58.9	20.18	01:59:58.46	–08:50:07.2	F606W
MACSJ0242.5–2132	17.80	02:42:35.94	–21:32:25.9	20.31	02:42:31.70	–21:31:06.7	F606W
MACSJ0257.6–2209	16.81	02:57:41.08	–22:09:17.7	18.09	02:57:37.01	–22:10:15.4	F814W
MACSJ0308.9+2645	17.89	03:08:55.93	+26:45:37.3	18.80	03:08:49.60	+26:45:56.1	F814W
MACSJ0404.6+1109	18.11	04:04:32.71	+11:08:04.7	18.19	04:04:33.67	+11:07:53.3	F814W
MACSJ0449.3–2848	19.74	04:49:20.72	–28:49:08.8	19.36	04:49:15.66	–28:49:08.7	F606W
MACSJ0451.9+0006	18.51	04:51:54.61	+00:06:18.2	18.94	04:51:53.99	+00:06:18.2	F814W
MACSJ0520.7–1328	19.13	05:20:42.05	–13:28:46.8	19.33	05:20:48.96	–13:29:38.1	F606W
MACSJ0521.4–2754	17.83	05:21:25.45	–27:54:53.2	18.51	05:21:25.54	–27:55:14.8	F814W
MACSJ0547.0–3904	17.68	05:47:01.52	–39:04:26.4	19.09	05:47:03.75	–39:04:35.0	F814W
MACSJ0600.1–2008	18.51	06:00:08.19	–20:08:09.2	19.24	06:00:10.25	–20:07:02.6	F814W
MACSJ0611.8–3036	16.75	06:11:50.21	–30:38:55.1	16.47	06:11:44.95	–30:37:00.8	F110W
MACSJ0712.3+5931	17.51	07:12:20.50	+59:32:20.4	18.67	07:12:20.61	+59:31:32.0	F814W
MACSJ0845.4+0327	17.79	08:45:27.77	+03:27:38.8	18.35	08:45:29.25	+03:27:28.4	F814W
MACSJ0913.7+4056	18.31	09:13:45.50	+40:56:28.5	20.73	09:13:35.53	+40:56:21.3	F606W
MACSJ0916.1–0023	17.90	09:16:09.24	–00:24:16.5	17.94	09:16:17.56	+00:24:05.9	F814W
MACSJ0947.2+7623	17.01	09:47:12.78	+76:23:13.6	19.73	09:47:14.43	+76:23:27.4	F814W
MACSJ0949.8+1708	18.09	09:49:51.80	+17:07:10.5	18.65	09:49:55.40	+17:06:38.4	F814W
MACSJ1006.9+3200	17.77	10:06:54.68	+32:01:32.0	18.60	10:06:55.27	+32:00:01.1	F814W
MACSJ1105.7–1014	19.51	11:05:46.80	–10:14:46.0	20.15	11:05:46.22	–10:14:24.7	F606W
MACSJ1115.2+5320	18.10	11:15:14.85	+53:19:54.3	18.93	11:15:18.75	+53:19:48.3	F814W
MACSJ1115.8+0129	19.26	11:15:51.89	+01:29:54.7	19.77	11:15:46.33	+01:29:39.2	F606W
MACSJ1124.5+4351	18.74	11:24:29.78	+43:51:25.5	19.30	11:24:38.23	+43:51:35.2	F814W
MACSJ1133.2+5008	18.09	11:33:13.17	+50:08:39.9	18.53	11:33:09.89	+50:08:18.9	F814W
MACSJ1141.6–1905	17.07	11:41:40.83	–19:05:15.5	17.03	11:41:40.60	–19:05:28.2	F110W
MACSJ1142.4+5831	16.69	11:42:24.80	+58:32:05.5	17.60	11:42:26.28	+58:32:43.4	F814W
MACSJ1206.2–0847	19.78	12:06:12.13	–08:48:03.3	20.05	12:06:05.37	–08:49:04.7	F606W
MACSJ1226.8+2153C	18.74	12:26:38.80	+21:53:22.7	18.88	12:26:40.79	+21:52:58.1	F814W
MACSJ1236.9+6311	17.54	12:36:58.72	+63:11:13.6	17.56	12:36:59.31	+63:11:11.5	F814W
MACSJ1258.0+4702	18.15	12:58:03.29	+47:02:57.6	18.34	12:58:02.09	+47:02:54.4	F814W
MACSJ1319.9+7003	17.34	13:20:08.40	+70:04:39.2	18.35	13:20:00.78	+70:03:15.1	F814W
MACSJ1328.2+5244	17.84	13:28:12.08	+52:43:18.8	17.98	13:28:15.69	+52:44:24.8	F814W
MACSJ1354.6+7715	18.09	13:54:42.72	+77:15:17.4	18.40	13:54:34.68	+77:15:48.5	F814W
MACSJ1359.1–1929	18.68	13:59:10.25	–19:29:24.8	19.50	13:59:09.01	–19:27:44.5	F814W
MACSJ1427.6–2521	17.41	14:27:39.47	–25:21:02.2	18.70	14:27:32.34	–25:21:37.6	F814W
MACSJ1447.4+0827	17.02	14:47:26.03	+08:28:24.7	19.37	14:47:25.76	+08:28:04.7	F814W
MACSJ1452.9+5802	17.69	14:52:57.49	+58:02:55.1	18.44	14:53:01.41	+58:03:24.4	F814W
MACSJ1526.7+1647	19.18	15:26:42.67	+16:47:38.7	20.21	15:26:41.03	+16:47:11.5	F606W
MACSJ1551.9–0207	17.56	15:51:58.47	–02:07:50.3	20.00	15:51:58.83	–02:08:14.8	F814W
MACSJ1621.3+3810	18.79	16:21:24.75	+38:10:08.8	19.40	16:21:22.55	+38:09:24.8	F814W
MACSJ1625.7–0830	19.39	16:25:45.92	–08:30:54.9	19.46	16:25:48.57	–08:32:02.6	F814W
MACSJ1644.9+0139	17.89	16:45:00.42	+01:39:57.0	17.94	16:45:01.22	+01:40:15.7	F814W
MACSJ1652.3+5534	17.69	16:52:18.71	+55:34:58.2	18.28	16:52:17.54	+55:34:56.7	F814W
MACSJ1731.6+2252	17.30	17:31:39.95	+22:51:58.5	18.54	17:31:41.73	+22:53:34.4	F814W
MACSJ1738.1+6006	17.78	17:38:06.89	+60:06:17.9	19.17	17:38:10.14	+60:05:52.5	F814W

Table 6. BCG and second brightest cluster members (selection as described in Section 4).

^a Magnitude uncertainties $\lesssim .01$. Magnitudes measured in F814W if available; else, in F606W, if available; else, in F110W. The band used for each cluster appears in the final column of the table.

ClusterBCG.....		G2.....			band
	mag ^a	RA	Dec	mag ^a	RA	Dec	
MACSJ1752.0+4440	18.43	17:51:53.39	+44:39:13.6	18.89	17:52:03.83	+44:39:44.0	F814W
MACSJ1806.8+2931	18.03	18:06:52.41	+29:30:12.7	19.21	18:06:47.52	+29:30:05.6	F814W
MACSJ2003.4-2322	17.34	20:03:36.77	-23:25:10.6	17.94	20:03:25.23	-23:24:57.0	F814W
MACSJ2046.0-3430	17.11	20:46:00.54	-34:30:17.9	16.60	20:45:59.37	-34:29:57.8	F110W
MACSJ2050.7+0123	17.70	20:50:43.15	+01:23:28.7	18.47	20:50:43.95	+01:23:31.7	F814W
MACSJ2051.1+0215	17.62	20:51:09.58	+02:16:13.7	17.70	20:51:12.27	+02:15:58.2	F814W
MACSJ2134.6-2706	17.50	21:34:36.00	-27:05:55.8	19.00	21:34:42.99	-27:06:18.7	F814W
MACSJ2135.2-0102	17.43	21:35:12.08	-01:02:58.7	18.31	21:35:09.69	-01:01:35.6	F814W
MACSJ2149.3+0951	18.36	21:49:19.66	+09:51:37.1	19.30	21:49:18.39	+09:51:58.7	F814W
MACSJ2211.7-0349	18.73	22:11:45.91	-03:49:44.7	20.43	22:11:45.82	-03:50:47.8	F606W
MACSJ2229.7-2755	16.24	22:29:45.22	-27:55:36.3	17.45	22:29:43.86	-27:55:25.0	F110W
MACSJ2241.8+1732	17.87	22:41:58.85	+17:31:40.3	17.67	22:41:56.25	+17:32:11.6	F814W
MACSJ2243.3-0935	20.49	22:43:19.83	-09:34:51.5	20.51	22:43:21.26	-09:35:10.4	F606W
MACSJ2245.0+2637	15.25	22:45:04.68	+26:38:04.8	17.58	22:45:10.31	+26:37:53.5	F110W
MACSJ2245.4+2808	17.82	22:45:27.76	+28:09:00.2	17.98	22:45:21.17	+28:07:05.8	F814W
SMACSJ0018.9-4051 ^b	20.12	00:19:01.54	-40:51:50.5	—	—	—	F606W
SMACSJ0040.8-4407 ^b	16.35	00:40:49.94	-44:07:51.0	—	—	—	F110W
SMACSJ0234.7-5831	18.78	02:34:50.76	-58:30:46.9	18.96	2:34:39.73	-58:30:16.8	F814W
SMACSJ0304.3-4401 ^b	20.09	03:04:16.85	-44:01:31.7	—	—	—	F606W
SMACSJ0332.8-8452 ^b	16.56	03:33:14.18	-84:53:25.2	—	—	—	F110W
SMACSJ0439.2-4600 ^b	18.73	04:39:13.96	-46:00:49.1	—	—	—	F606W
SMACSJ0549.3-6205	17.90	05:49:19.98	-62:05:13.6	18.02	5:49:13.35	-62:06:12.5	F814W
SMACSJ0600.2-4353	17.27	06:00:12.96	-43:53:29.4	18.11	6:00:19.12	-43:54:12.3	F814W
SMACSJ0723.3-7327	19.14	07:23:18.42	-73:27:17.2	19.21	7:23:20.48	-73:25:50.1	F814W
SMACSJ1519.1-8130 ^b	20.72	15:18:54.97	-81:30:23.7	—	—	—	F606W
SMACSJ2031.8-4036	17.77	20:31:47.82	-40:36:54.3	18.25	20:31:53.28	-40:37:30.4	F814W
SMACSJ2131.1-4019	18.10	21:31:04.95	-40:19:21.2	19.42	21:31:03.56	-40:19:05.3	F814W
SMACSJ2332.4-5358 ^b	16.75	23:32:27.52	-53:58:28.1	—	—	—	F110W

Table 6 – *continued* BCG and second brightest cluster members (selection as described in Section 4).

^a Magnitude uncertainties $\lesssim .01$. Magnitudes measured in F814W if available; else, in F606W, if available; else, in F110W. The band used for each cluster appears in the final column of the table.

^b Colour information not available (from either *HST* or ground-based imaging); thus distinguishing BCG and G2 from foreground galaxies is problematic. For these clusters we present our BCG identification tentatively, and we decline to identify G2.